Center for Computational Engineering Science Mathematics Division

RWTH AACHEN UNIVERSITY

Diese Arbeit wurde vorgelegt am
Lehrstuhl für Mathematik (MathCCES)

Application of the Adjoint Method in Gradient-based Optimization to the $\mathcal{M}1$-Model in Electron Beam Microanalysis

Bachelor Thesis

Computational Engineering Science

Vorgelegt von
Presented by

Tamme Claus
tamme.claus@rwth-aachen.de
RWTH Aachen University

Prüfer
Examiner

Prof. Dr. Manuel Torrilhon
Lehrstuhl für Mathematik (MathCCES)
RWTH Aachen University

Betreuer
Supervisor

Jonas Bünger
Lehrstuhl für Mathematik (MathCCES)
RWTH Aachen University

communicated by

Prof. Dr. Manuel Torrilhon
Lehrstuhl für Mathematik (MathCCES)
RWTH Aachen University

September 2018

Abstract

The spatial resolution of electron probe microanalysis is currently restricted to a volume larger than the volume of interaction between beam electrons and the sample, because the utilized models to predict k-ratios assume a homogeneous chemical composition inside that volume. The chemical composition of the sample is reconstructed by solving the inverse problem of finding the composition such that a model best reproduces the k-ratios measured within the experiment. To improve the spatial resolution, more sophisticated modeling of the k-ratios is necessary. In this work, a model to calculate k-ratios based on the $\mathcal{M}1$-Model is considered. The $\mathcal{M}1$-Model is solved using the finite volume library CLAWPACK and the inverse problem is investigated for spatially varying chemical compositions within the interaction volume. Furthermore the inverse problem for a particular sample is solved using iterative gradient based optimization methods in combination with the adjoint state method to calculate gradients.

Zusammenfassung

Die räumliche Auflösung der Elektronenstrahlmikroanalyse ist derzeit beschränkt auf ein Volumen, das größer ist als das Interaktionsvolumen zwischen Strahlelektronen und der Probe, da die verwendeten Modelle zur Berechnung der k-Ratios eine homogene chemische Zusammensetzung innerhalb des Interaktionsvolumens annehmen. Die chemische Zusammensetzung der Probe wird berechnet, indem das inverse Problem des Auffindens einer Zusammensetzung gelöst wird, sodass ein Modell die experimentell bestimmten k-Ratios möglichst gut reproduziert. Um die räumliche Auflösung zu verbessern müssen ausgefeiltere Modelle zur Berechnung der k-Ratios benutzt werden. In dieser Arbeit wird ein k-Ratio Modell betrachtet, das auf dem $\mathcal{M}1$-Modell basiert. Das $\mathcal{M}1$-Modell wird mithilfe der Finite-Volumen Bibliothek CLAWPACK gelöst und das inverse Problem wird für innerhalb des Interaktionsvolumens variierende chemische Zusammensetzungen untersucht. Außerdem wird das inverse Problem anhand einer Beispielprobe mithilfe iterativer gradienten-basierter Optimierungsmethoden in Verbindung mit der Adjungiertenmethode zur Berechnung der Gradienten gelöst.

Contents

Introduction **1**

1 Electron Probe Microanalysis **2**
1.1 Mass Concentration and Density . . . 3
1.2 Ionization Cross Section . . . 4
1.3 Fluorescence Yield . . . 5
1.4 Mass Attenuation . . . 6
1.5 Detector Intensity . . . 6
1.6 K-Ratios . . . 7
1.7 The Inverse Problem . . . 7

2 Modeling the Electron Fluence **8**
2.1 $\mathcal{M}1$-Model . . . 8
2.1.1 Derivation . . . 8
2.1.2 $\mathcal{M}1$-Model . . . 8
2.1.3 Electron Beam as Initial or Boundary Condition . . . 12
2.1.4 $\mathcal{M}1$-Model as a Constraint to the Optimization Problem . . . 13
2.2 The Finite Volume Method in CLAWPACK . . . 14
2.2.1 Riemann Problem . . . 14
2.2.2 Wave Propagation Method . . . 17
2.2.3 2D Implementation in CLAWPACK . . . 21
2.3 Evaluation of the $\mathcal{M}1$-Model . . . 22

3 Solving the Inverse Problem **26**
3.1 Analysis of the Objective Function . . . 26
3.2 Optimization . . . 30
3.2.1 Gradient Based Optimization . . . 31
3.2.2 Gradient of the Objective Function . . . 31
3.2.3 Finite Difference Approximation . . . 31
3.2.4 Adjoint Gradient Calculation . . . 32
3.3 Adjoint Equations for the $\mathcal{M}1$-Model . . . 34
3.3.1 Forward Equation . . . 34
3.3.2 Adjoint Equation . . . 35
3.3.3 Scalar Product . . . 38
3.4 Optimization using the Adjoint Method . . . 39

Conclusion and Outlook **41**

References **42**

List of Figures

1 Sketch of EPMA 2
2 Energy levels of nickel with subshells and Kα, Kβ transitions 3
3 Stopping power for homogeneous elements 10
4 Transport coefficient for homogeneous elements 11
5 Linear scalar advection at $t = 0$ and $t = \tilde{t}$ 15
6 Propagation of waves originating from a single discontinuity 16
7 Plot of the solution at $t = 0$(solid) and $t = 1$(dashed) 17
8 Three cells C_{i-1}, C_i, C_{i+1} 18
9 The electron fluence at different energies 23
10 Characteristic x-ray intensities of nickel and chromium 24
11 Plot of the FV energy steps and the beam intensity 24
12 Objective function for a homogeneous material of nickel and chromium 27
13 Objective function for a vertically divided material of nickel and chromium 28
14 Four variable cells, the positions of the beam and the impact zones of the electrons 28
15 Objective function varying p_0 and p_2 29
16 Objective function varying p_0 and p_1 29
17 Impact zone of the electrons for different densities 30
18 Gradient of the objective function of a homogeneous material 39
19 Plot of the errors for each iteration step of the optimization 40
20 The iteration steps of the optimization 40

List of Tables

1 Tabulated coefficients for the fluorescence yield 5
2 Tabulated coefficients for the Eddington factor 12

Introduction

Motivation The chemical composition of solid materials is a quantity of interest in many fields of research. In geophysics the components of minerals are investigated to understand their origin and formation, as well as to predict their utilization. Even meteorites are analysed to figure out their origin. But most commonly it is of interest in engineering and material science to make predictions about material properties, to perform fracture analysis or quality control.

Electron probe microanalysis (EPMA) is a method to determine the chemical composition of solid materials on a micro scale without destroying its structure. A material sample gets excited by a focused electron beam, causing the atoms to emit x-rays. The intensity of generated characteristic x-rays is measured by a detector and normalized to so-called k-ratios. The composition of the sample is reconstructed by solving the inverse problem of finding the specific set of chemical compositions such that a mathematical model reproduces the k-ratios measured within the experiment best.

Currently the spatial resolution of EPMA is restricted to a volume larger than the volume of interaction between beam electrons and the sample, because all models used for reconstruction assume homogenity or a layered structure inside that volume[4]. To resolve mass concentrations on a scale smaller than the interaction volume, more sophisticated models, that allow inhomogeneous composition within the interaction volume, are neccessary. The goal of this work is the analysis and solution of the inverse problem using a model based on the $\mathcal{M}1$-Model[18], to reproduce the k-ratios.

Overview Section 1 shows how k-ratios can be calculated from the electron fluence inside the material. The quantities mass concentration and density are introduced and the physical processes taking place inside the sample are described. In addition, the inverse problem is specified mathematically which involves the definition of an objective function.

The computation of the electron fluence using the $\mathcal{M}1$-Model is discussed in section 2. Section 2.1 describes the individual parts of the model and the modeling of the electron beam as an initial or boundary condition. In addition, the $\mathcal{M}1$-Model is formulated as a constraint to the objective function. Section 2.2 explains the finite volume method (FVM) which we use to solve the $\mathcal{M}1$-Model and presents the implementation of the $\mathcal{M}1$-Model in the FV-library CLAWPACK. Based on this implementation, section 2.3 shows a numerical evaluation of the $\mathcal{M}1$-Model.

Section 3 deals with the solution of inverse problem. Section 3.1 investigates the convexity of the objective function with respect to different chemical compositions, detector positions, as well as beam positions and energies. Section 3.2 briefly describes gradient based optimization methods to solve the inverse problem and the fast and accurate gradient calculation using the adjoint state method. In section 3.3 the adjoint state method is applied to our objective function. Finally in section 3.4 the implementation of the adjoint state method is validated and the chemical composition of an sample is reconstructed with high resolution.

1 Electron Probe Microanalysis

In electron probe microanalysis the goal is to determine the chemical composition of solid materials. For that purpose the fluorescence property of chemical elements, e.g. copper, nickel or chromium are exploited. The specimen whose chemical composition is to be determined, is bombarded with electrons generated by a electron source, that are accelerated and focussed as a beam. A sketch of the method is shown in figure 1.

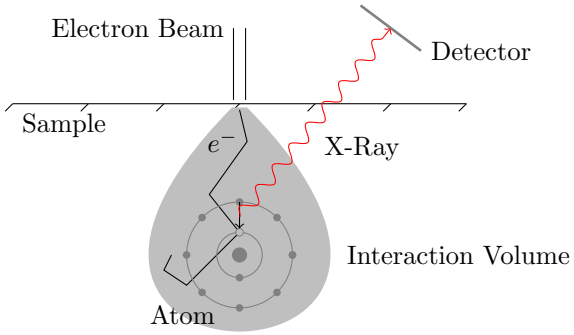

Figure 1: Sketch of EPMA

Electrons enter the sample and interact with the atoms inside the specimen. The physical processes generating x-radiation inside the sample are bremsstrahlung and characteristic radiation. Bremsstrahlung is generated by the deceleration of the electrons when interacting with the positive charged atom nuclei inside the specimen. The energy lost due to deceleration is emitted as x-rays, therefore the spectrum is continuous and acts like a background noise in EPMA[18] and will not be further regarded here.

Characteristic radiation results from beam electrons exciting inner shell electrons from atoms inside the specimen. An atom gets ionized with a vacancy on its inner shell, which leaves it in an excited state and it relaxes by filling the inner shell vacancy with an outer shell electron. The energy loss of the electron falling from an outer onto an inner shell leads to the emittation of a x-ray whose wavelength corresponds to the energy loss. As energy levels of electron shells are characteristic for each atom, such x-rays are likewise characteristic and provide information on the chemical composition of the specimen. Traveling through the material a part of the x-rays gets absorbed, the remaining part is emitted and can be measured on a detector.

The energy levels of nickel with its shells K,L,M and subshells I - IV are shown in figure 2. The arrows symbolise the transitions, the relaxiation by falling from a higher subshell, Kα and Kβ.

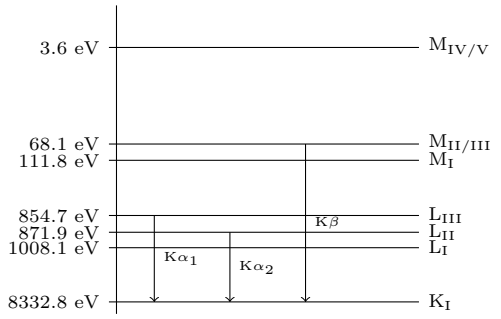

Figure 2: Energy levels of nickel with subshells and Kα, Kβ transitions

In this section we will introduce the physical quantities mass concentration and mass density, which define the chemical composition of the sample and are the quantities to be reconstructed. Building upon them and the electron fluence, which is the topic of section 2, we peruse the physical processes occurring inside the sample. The section is finished with the calculation of k-ratios, the quantity measured from experiments and the definition of the inverse problem that arises in electron probe microanalysis.

1.1 Mass Concentration and Density

In a solid material sample of volume Ω consisting of multiple chemical elements the mass concentration is defined using an infinitesimally small control volume $d\bar{x}$ around the position $\bar{x} \in \Omega$. For the total mass inside this control volume we write m^{tot} and for the partial mass of each element m^i. The mass concentration of an element i inside $d\bar{x}$ is

$$c^i = \frac{m^i}{m^{tot}} \ . \tag{1.1}$$

Mass is always positive and the sum of all partial masses has to add up to $\sum_i m^i = m^{tot}$. Therefore we impose two constraints on the mass concentration

$$c^i \geq 0 \quad \text{and} \quad \sum_i c^i = 1 \ . \tag{1.2}$$

Therefore only $m-1$ mass concentrations can be chosen in an sample of m elements, such that for the last element m the mass concentration is

$$c^m = 1 - \sum_i^{m-1} c^i \ . \tag{1.3}$$

Due to the formation of various atomic structures during the production of the material sample, also the density varies

$$\rho = \frac{m^{tot}}{d\bar{x}} \ . \tag{1.4}$$

We want to locally resolve both quantities, so the mass concentrations and the density are functions of the position $\bar{x}$

$$c^i(\bar{x}) : \Omega \to \mathbb{R} \qquad \rho(\bar{x}) : \Omega \to \mathbb{R} \ . \tag{1.5}$$

Additionally we will define the partial density of an element i as

$$\rho^i(\bar{x}) = \frac{m^i}{d\bar{x}} = c^i(\bar{x})\rho(\bar{x}) \ . \tag{1.6}$$

As we later want to approximate density and mass concentration numerically, we need to discretise them. In this work we model the material in two spatial dimensions, so we can approximate mass concentrations and density as a piece-wise constant function on grid cells T^j

$$c^i(\bar{x}) = c^i_j \text{ if } \bar{x} \in T^j \tag{1.7}$$

$$\rho(\bar{x}) = \rho_j \text{ if } \bar{x} \in T^j \ . \tag{1.8}$$

In this work the quantities mass concentration and density are also referred to as parameters. As a mathematical quantity we define both collectively in one parameter vector p

$$p = \begin{pmatrix} c^0_0 \\ \vdots \\ c^{m-1}_0 \\ c^0_1 \\ \vdots \\ c^{m-1}_1 \\ \vdots \\ \rho_0 \\ \vdots \end{pmatrix} \begin{matrix} \left.\begin{matrix} \\ \\ \\ \end{matrix}\right\} \text{mass concentrations of grid cell } T^0 \\ \left.\begin{matrix} \\ \\ \\ \end{matrix}\right\} \text{mass concentrations of grid cell } T^1 \\ \left.\begin{matrix} \\ \end{matrix}\right\} \text{mass concentrations of grid cells } T^{2,\cdots} \\ \left.\begin{matrix} \\ \\ \end{matrix}\right\} \text{densities of all grid cells } T^j \end{matrix} \ . \tag{1.9}$$

1.2 Ionization Cross Section

In this section we assume that the angular-average electron fluence $\psi^0(\bar{x}, \epsilon)$ at energy ϵ and position $\bar{x}$ is known as it will be the topic of section 2. Based on mass concentraions, density and the electron fluence we now derive the detected intensity of x-rays.

The reason for the ionization of an atom is the collision with electrons. The number of electrons hitting an atom of element i can be denoted by

$$N^i_V(\bar{x})\psi^0(\bar{x}, \epsilon) \ , \tag{1.10}$$

where the number of atoms of element i per cubic meter $N^i_V(\bar{x})$ is

$$N^i_V(\bar{x}) = \rho^i(\bar{x})\frac{N_A}{A^i} \ , \tag{1.11}$$

with $\rho^i(\bar{x})$ the partial density, A^i the atomic mass of element i and N_A Avogadro's constant.

Only a fraction of those collisions lead to ionization of atoms. The fraction is called the ionization cross section σ_{ion}. It is specific to each element and we also have to distinguish the subshells, as the released energy differs (see figure 2). In this work we will only consider ionization of K-shell (the

innermost shell) electrons, so $\sigma_{ion}^{i,j}$ denotes the fraction of ionization events leading to a electron transition j (e.g $K\alpha_1$). $\sigma_{ion}^{i,j}$ is given in [24] with

$$\sigma_{ion}^{i,j}(\epsilon) = \frac{Z_K a_H^2 F R^2 \Psi \Phi \ln \upsilon}{E_K^2 \upsilon} \ , \tag{1.12}$$

where $\upsilon = \frac{\epsilon}{E_K}$ is the ratio of beam electon energy ϵ to edge energy E_K of the bound electrons. Z_K is the ground state occupancy of the shell, a_H the Bohr radius and R the Rydberg energy. The other quantities are

$$\Psi = \left(\frac{E_K}{R}\right)^{(-0.0318+\frac{0.3160}{\upsilon}-\frac{0.1135}{\upsilon^2})} \tag{1.13}$$

$$\Phi = 10.57 e^{-\frac{1.736}{\upsilon}+\frac{0.317}{\upsilon^2}} \tag{1.14}$$

$$F = \left(\frac{2+I}{2+T}\right)\left(\frac{1+T}{1+I}\right)^2\left(\frac{(I+T)(2+T)(1+I)^2}{T(2+T)(1+I)^2+I(2+I)}\right)^{3/2} \tag{1.15}$$

$$I = \frac{E_K}{mc^2} \tag{1.16}$$

$$T = \frac{\epsilon}{mc^2} \ . \tag{1.17}$$

1.3 Fluorescence Yield

Besides from releasing the energy, which got availiable from the electron transition, as an x-ray, there is the chance of releasing the energy by the ejection of another electron from an outer shell. This is called the Auger effect. For x-ray radiation this means, that only a fraction of ionization events leads to x-ray emission. This fraction is called fluorescence yield ω.

As our interest lies in ionization events of the K-shell only, the fluorescence yield of the K-shell ω_K will be considered here. An approximation of ω_K^i by a polynomial in the atomic number Z^i, is given by [10] [11]

$$\omega_K^i = \sum_{n=0}^{4} \alpha_n (Z^i)^n \ , \tag{1.18}$$

with experimentally determined coefficients α_n given in Table 1.

a_n	a_0	a_1	a_2	a_3	a_4
$Z \in [11, 19]$	$1.4340e^{-1}$	$-2.5606e^{-2}$	$1.3163e^{-3}$	0	0
$Z \in [20, 99]$	$-7.6388e^{-1}$	$5.4070e^{-2}$	$-4.0544e^{-4}$	$-1.4348e^{-6}$	$1.8252e^{-8}$

Table 1: Tabulated coefficients for the fluorescence yield

Combined with the ionization cross section this yields the fraction of collisions resulting in the generation of characteristic x-rays

$$\sigma_{emiss}^{i,j}(\epsilon) = \omega_K^i \sigma_{ion}^{i,j}(\epsilon) \ . \tag{1.19}$$

We obtain the intensity $I^{0,i,j}$ of generated x-rays j characteristic for element i generated at position

$\bar{x}$ from integration over all energies

$$I^{0,i,j}(\bar{x}) = N_V^i(\bar{x}) \int_\epsilon \sigma_{emiss}^{i,j}(\epsilon)\psi^0(\bar{x},\epsilon)\,\mathrm{d}\epsilon \ . \tag{1.20}$$

1.4 Mass Attenuation

While traveling through the material the x-rays get attenuated according to Beer-Lambert's law[30]

$$\frac{\mathrm{d}I^{i,j}(\bar{x})}{\mathrm{d}\bar{x}} = -\mu(\bar{x}, E^{i,j})I^{i,j}(\bar{x}) \ . \tag{1.21}$$

The linear attenuation coefficient $\mu(\bar{x}, E^{i,j})$ in a compound is defined in [12] as

$$\mu(\bar{x}, E^{i,j}) = \sum_k c^k(\bar{x})\rho(\bar{x}) \left(\frac{\mu}{\rho}\right)^k_{E^{i,j}} = \sum_k \rho^k(\bar{x}) \left(\frac{\mu}{\rho}\right)^k_{E^{i,j}} \tag{1.22}$$

where $\left(\frac{\mu}{\rho}\right)^k_{E^{i,j}}$ is the mass attenuation coefficient specific to element k, which also depends on the x-ray energy $E^{i,j}$. The mass attenuation coefficients have been determined by experiments and are tabulated in [12].

To model the mass attenuation of x-rays generated at $\bar{x}$, we define a linear path from each position $\bar{x}$ inside the specimen to the detector $\bar{x}_d$

$$d(\bar{x}) = \{\bar{x} + \lambda(\bar{x}_d - \bar{x}), \lambda \in [0,1]\} \ . \tag{1.23}$$

The intensity on the detector then reads

$$I^{0,i,j}(\bar{x}) e^{-\int_{d(\bar{x})} \mu(y,E^{i,j})\,\mathrm{d}y} \ , \tag{1.24}$$

which is a solution to Beer-Lambert's law.

1.5 Detector Intensity

To calculate the detected intensity we need to take x-rays generated at all positions into account. Thereby the total intensity of x-rays j characteristic to element i is given by the integral over the whole domain Ω

$$\begin{aligned} I^{i,j} &= \int_\Omega I^{0,i,j}(\bar{x}) e^{-\int_{d(\bar{x})} \mu(y,E^{i,j})\,\mathrm{d}y}\,\mathrm{d}\bar{x} \\ &= \int_\Omega N_V^i(\bar{x}) e^{-\int_{d(\bar{x})} \mu(y,E^{i,j})\,\mathrm{d}y} \int_\epsilon \sigma_{emiss}^{i,j}(\epsilon)\psi^0(\bar{x},\epsilon)\,\mathrm{d}\epsilon\,\mathrm{d}\bar{x} \ . \end{aligned} \tag{1.25}$$

This assumes that every x-ray generated inside the specimen travels towards the detector or every x-ray leaving the sample gets detected. A legit assumption because the generated x-rays do not have a preferred direction and the intensities will be normalized later (k-ratios).

1.6 K-Ratios

The fraction of detected x-rays is proportional to the size of the detector. But also additional uncertainties, e.g. the efficiency of the detector influence $I^{i,j}$. Those uncertainties can be eliminated if we normalize the intensities using standard intensities I_{std} measured by the same experimental setup but with samples which chemical composition is known. The normalized intensities are called k-ratios.

$$k^{i,j} = \frac{I^{i,j}}{I^{i,j}_{std}} \ . \tag{1.26}$$

In this work only artificial measurements from simulations of the experiment were used instead of real experiments. The uncertainties were not modeled by the simulation, therefore we can neglect them here and calculate the k-ratios using $I^{i,j}_{std} = const.$

In EPMA an experiment is typically conducted with multiple beam energies and beam positions. Especially for the spatial resolution, the inclusion of multiple beam positions is important. For various positions, the electrons interact in different parts of the sample and all of these experiments yield different k-ratios. Therefore we introduce a new subscript $\cdot_{ex}$ which indicates the relation of different quantities to a specific experiment. The k-ratio for an experiment ex, x-ray j of element i is called $k^{i,j}_{ex}$. The k-ratio $k^{i,j}_{ex}$ is a function of the parameters p, but for the sake of clarity I drop the parenthesis (p).

1.7 The Inverse Problem

Previously we have shown how to calculate k-ratios $k^{i,j}_{ex}$ from the electron fluence (section 2) and the samples mass concentration and density. Given this mathematical model, we now want to take actual measurements of the k-ratios into account. We call the measured k-ratios $\tilde{k}^{i,j}_{ex}$.

To quantify the difference of measured and simulated k-ratios, we define a objective function

$$J(p) = \sum_{ex} J_{ex}(p) = \sum_{ex,i,j} \frac{1}{2}(k^{i,j}_{ex} - \tilde{k}^{i,j}_{ex})^2 \ . \tag{1.27}$$

This is the least squares error of the simulated k-ratios with respect to the measured k-ratios. As the simulated k-ratios depend on the parameters, the objective function is a function of the parameters p. Per definition the objective function is ≥ 0. If the objective function is minimal we consider the related parameters to this minimum as the real mass concentrations and density.

We formulate the inverse problem of reconstructing the chemical composition of the material sample as a minimization problem of the least-squares error (1.27): Find the parameter set p^*, such that

$$p^* = \arg\min_p J(p) = \arg\min_p \sum_{ex,i,j} \frac{1}{2}(k^{i,j}_{ex} - \tilde{k}^{i,j}_{ex})^2 \ . \tag{1.28}$$

2 Modeling the Electron Fluence

The derivation of the equations for the intensities/k-ratios (equation (1.25)) assumed that the electron fluence $\psi^0(\bar{x}, \epsilon)$ inside the sample is known. It mainly determines the creation of x-radiation.

In section 2.1 the $\mathcal{M}1$-Model will be introduced, a mathematical model to describe angular moments of the electron density distribution function resolved in position and energy. It will also be incorporated into the inverse problem by formulating it as a constraint. In section 2.2 the finite volume method, which is used to solve the $\mathcal{M}1$-Model, is presented together with the framework CLAWPACK, a Python/Fortran finite volume library. Finally we present numerical experiments in section 2.3.

2.1 $\mathcal{M}1$-Model

The description of the $\mathcal{M}1$-Model is subdivided in a brief derivation in section 2.1.1, a detailed analysis of the terms of the model in section 2.1.2 and the relation to the electron beam in section 2.1.3. Then we take up the inverse problem again to incorporate the model into it.

2.1.1 Derivation

The $\mathcal{M}1$-Model is derived from the Boltzmann Transport Equation[18], which describes the evolution of a thermodynamic particle system. In our case that is the electrons inside the sample. Rather than describing each particle independently, they are interpreted as a statistical quantity on a larger scale. To calculate the k-ratios, the quantity of interest is the angular-average electron fluence ψ^0, which is a function of space $\bar{x}$ and energy ϵ. Its progression is governed by advection of electrons in space and scattering with the background medium (in our case e.g. metal atoms). The Boltzmann equation handles these discontinuous events averaged, such that predictions for the electron fluence are possible.

Using a continuous-slowing-down approximation for the energy loss of the electrons, the equation can be further simplified[18]. In EPMA it is also possible to consider the stationary state, as it arises quickly after the initial beam exposure. The initial phase can be neglected over the whole irradiation period.

The $\mathcal{M}1$-Model, which will be used to calculate the electron fluence in this work, is a moment approximation of these equations with a minimum entropy closure after the first moment. A detailed derivation and justification of the closure of the $\mathcal{M}1$-Model can be found in [6] [18] [19] [23].

2.1.2 $\mathcal{M}1$-Model

The $\mathcal{M}1$-Model(2D) is a hyperbolic partial differential equation given by

$$\begin{aligned} -\partial_\epsilon(S(\bar{x},\epsilon)U(\bar{x},\epsilon)) + \partial_x F_x(U(\bar{x},\epsilon)) + \partial_y F_y(U(\bar{x},\epsilon)) &= -T(\bar{x},\epsilon)U(\bar{x},\epsilon) \\ \forall \bar{x} \in \Omega, \epsilon \in [\epsilon_{cutoff}, \epsilon_{initial}] \ , \end{aligned} \tag{2.1}$$

where S is the stopping power, T the transport coefficient and F are flux functions. In this work we will consider two spatial dimensions, so the physical domain is $\Omega \subset \mathbb{R} \times \mathbb{R}$ and is defined as

$\Omega = [x_0, x_1] \times [y_0, y_1]$. The energy ϵ lies in an interval $[\epsilon_{cutoff}, \epsilon_{initial}]$, where the cutoff energy ϵ_{cutoff} typically is chosen lower than the minimal energy needed to ionize any element inside the specimen. The initial energy $\epsilon_{initial}$ has to be chosen greater of equal than the energy of beam electrons, such that the whole process can be modelled.

The state variable $U \colon \Omega \times [\epsilon_{cutoff}, \epsilon_{initial}] \to \mathbb{R}^3$, is defined as

$$U(\bar{x}, \epsilon) = \begin{pmatrix} \psi^0(\bar{x}, \epsilon) \\ \psi^1_x(\bar{x}, \epsilon) \\ \psi^1_y(\bar{x}, \epsilon) \end{pmatrix} = \begin{pmatrix} u_1(\bar{x}, \epsilon) \\ u_2(\bar{x}, \epsilon) \\ u_3(\bar{x}, \epsilon) \end{pmatrix} , \tag{2.2}$$

where ψ^0 denotes the zeroth moment, the angular-average electron fluence and ψ^1 the first moment.

In the following paragraphs the individual terms and quantities of the model equation (2.1), such as the stopping power S, the flux functions F_x and F_y and the transport coefficient T will be introduced and explained. To define the mathematical problem uniquely, initial and boundary conditions are necessary. They and their correlation to the electron beam are dealt with in the next section 2.1.3.

Stopping Power The term $-\partial_\epsilon(S(\bar{x}, \epsilon)U(\bar{x}, \epsilon))$ follows from modelling the energy loss of electrons as a continuous process, where the stopping power S describes the average energy loss of electrons travelling with energy ϵ. The stopping power for a compound is given in [18] as

$$S(\bar{x}, \epsilon) = \rho(\bar{x}) \sum_i \frac{c^i(\bar{x})}{A^i} \frac{2\pi e^4 Z^i}{(4\pi\epsilon_0)^2 \epsilon} \ln(b\frac{\epsilon}{J^i}) , \tag{2.3}$$

where ρ is the density and c^i is the mass concentration. The remaining quantities are constants: the vacuum permittivity ϵ_0, the elementary charge e, a relativistic constant $b = \sqrt{\frac{e}{2}}$ as well as the atomic mass A^i and the atomic number Z^i.

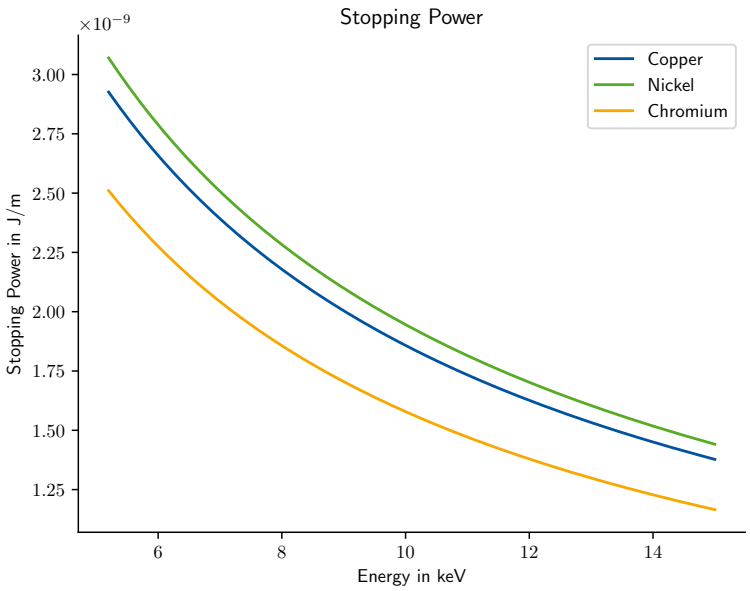

Figure 3: Stopping power for homogeneous elements

The mean ionization potential J^i for an element i can be calculated from its atomic number Z^i

$$J^i = e \begin{cases} 9.76Z^i + 58.8(Z^i)^{-0.19} & , Z > 6 \\ 11.5Z^i & , Z \leq 6 \end{cases} . \tag{2.4}$$

Figure 3 shows the stopping power for copper, nickel and chromium on a energy range from 5 to 15keV.

Transport Coefficient The source term on the right hand side $-T(\bar{x}, \epsilon)U(\bar{x}, \epsilon)$ with

$$T\left(x,t\right) = \text{diag}\left(0, T_{in+el}\left(x,t\right), T_{in+el}\left(x,t\right)\right) \tag{2.5}$$

is called the inelastic and elastic transport coefficient. In our application elastic collisions dominate the changes in the direction of electron movement, therefore we neglect the inelastic transport coefficient[18]. It can be calculated by

$$\begin{aligned} &T_{in+el}(\bar{x}, \epsilon) \approx T_{el}(\bar{x}, \epsilon) \\ =&\frac{2\pi e^4 \rho(x)}{16(4\pi\epsilon_0)^2\epsilon^2} \sum_i \frac{c^i(x)(Z^i)^2}{A^i} \\ &\left(\frac{8}{\cos(\theta_0^i(\epsilon)) - 3} + 4(\ln(3 - \cos(\theta_0^i(\epsilon))) - \ln(1 - \cos(\theta_0^i(\epsilon)))) \right) , \end{aligned} \tag{2.6}$$

where θ_0^i is the screening angle, R^i is the screening radius and λ the de Broglie wavelength

$$\theta_0^i(\epsilon) = \frac{\lambda(\epsilon)}{2\pi R^i} , \quad R^i = a_H (Z^i)^{-1/3} , \quad \lambda\left(\epsilon\right) = \frac{h}{\sqrt{2m_0\epsilon}} . \tag{2.7}$$

Constants used in this equations are the Bohr radius a_H, Planck's constant h, the electron rest mass m_0, the elementary charge e and the vacuum permittivity ϵ_0. In figure 4 the transport coefficient is shown for copper, nickel and chromium.

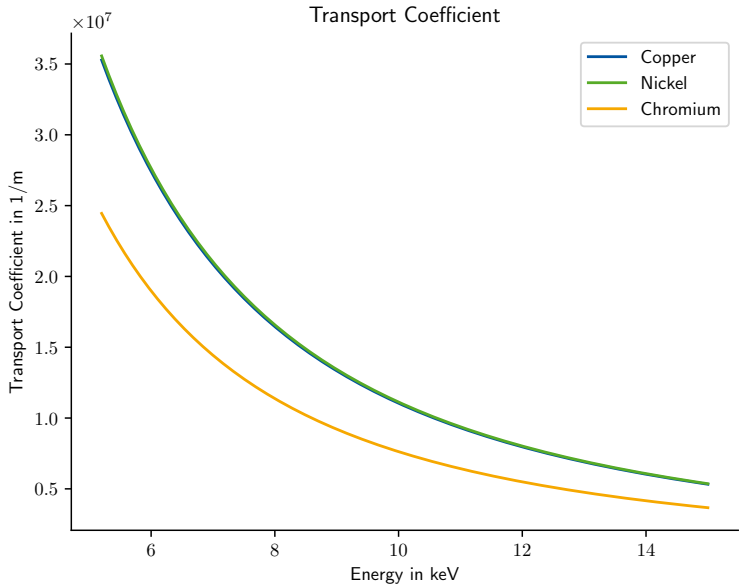

Figure 4: Transport coefficient for homogeneous elements

Flux Function The mathematical flux functions for a two dimensional system are given by

$$F_x(U) = \begin{pmatrix} u_1 \\ u_0\left(\frac{1-\chi(|\alpha|)}{2} + \frac{u_1^2}{u_1^2+u_2^2}\frac{3\chi(|\alpha|)-1}{2}\right) \\ u_0\left(\frac{u_1u_2}{u_1^2+u_2^2}\frac{3\chi(|\alpha|)-1}{2}\right) \end{pmatrix} \tag{2.8}$$

$$F_y(U) = \begin{pmatrix} u_2 \\ u_0\left(\frac{u_1u_2}{u_1^2+u_2^2}\frac{3\chi(|\alpha|)-1}{2}\right) \\ u_0\left(\frac{1-\chi(|\alpha|)}{2} + \frac{u_2^2}{u_1^2+u_2^2}\frac{3\chi(|\alpha|)-1}{2}\right) \end{pmatrix} , \tag{2.9}$$

where χ is the Eddington factor. The mathematical flux $F(U)$ couples the equations for u_1, u_2 and u_3. To calculate the Eddington factor, we need to define the anisotropy parameter

$$\alpha = \frac{\psi^1}{\psi^0} = \frac{1}{u_1}\begin{pmatrix} u_2 \\ u_3 \end{pmatrix} \tag{2.10}$$

and its length

$$|\alpha| = \frac{\sqrt{u_2^2+u_3^2}}{u_1} . \tag{2.11}$$

In [18] it has been proven, that the anisotropy parameter is bounded by $|\alpha| \leq 1$. The Eddington factor implicitly depends on $|\alpha|$ and will be approximated[18] by a rational function in $|\alpha|$

$$\chi(|\alpha|) \approx \frac{a_6|\alpha|^6 + a_4|\alpha|^4 + a_2|\alpha|^2 + a_0}{|\alpha|^4 + b_2|\alpha|^2 + b_0} . \tag{2.12}$$

The coefficients a_i and b_i are given in table 2.

i	6	4	2	0
a_i	0.720371	-0.139318	0.348509	0.621529
b_i	-	-	-1.32002	1.87095

Table 2: Tabulated coefficients for the Eddington factor

2.1.3 Electron Beam as Initial or Boundary Condition

Until now the developed model only describes the electron interactions inside the specimen, but we also need to model the electrons from the beam. As they enter from outside the specimen, the obvious idea is to use boundary conditions.

For the $\mathcal{M}1$-Model there are two possibilities considered here, one modeling the beam as a boundary condition, another modeling it as an initial condition.

Boundary Condition We assume, that the beam electrons are normally distributed in energy, so we can write the intensity of electrons as

$$I(\epsilon) = e^{(-b_\epsilon(\epsilon-\epsilon_{beam})^2)} \ . \tag{2.13}$$

In this equation ϵ_{beam} is the beam energy and b_ϵ is a constant, which defines the beams variance in energy. The beam hits the sample from positive x direction and is assumed to be normally distributed in its spatial dimension, so as a boundary condition we suggest

$$U(\bar{x},\epsilon) = \begin{pmatrix} I(\epsilon)e^{(-b_x(x-x_{beam})^2)} \\ -I(\epsilon)e^{(-b_x(x-x_{beam})^2)} \\ 0 \end{pmatrix} \quad x \in \delta\Omega \ . \tag{2.14}$$

x_{beam} is the x-position of the beam center, x is the first component of $\bar{x} = \begin{pmatrix} x \\ y \end{pmatrix}$ and b_x defines the width of the beam. Due to the boundary condition for the first moment ψ^1 the beam electrons move only in negative x-direction. ψ^1 is chosen as large as possible, but must not violate the condition $|\alpha| \leq 1$. The boundary condition (equation(2.14)) should only be set on the boundary where electrons enter the sample, otherwise $U(\bar{x} \in \delta\Omega, \epsilon) = 0$.

The initial state is $U(\bar{x}, \epsilon = \epsilon_{initial}) = 0$ in this case, which means that no electrons with $\epsilon_{initial}$ are in the material. The initial energy should be chosen $\epsilon_{initial} > \epsilon_{beam}$, such that $I(\epsilon_{initial}) \approx 0$ and the boundary condition does not introduce a discontinuity.

Initial Condition Another approach is to model the beam as an initial condition $\epsilon_{initial} = \epsilon_{beam}$

$$U(\bar{x}, \epsilon = \epsilon_{initial}) = \begin{pmatrix} e^{(-b_x(x-x_{beam})^2)}e^{(-b_y(y-y_{beam})^2)} \\ 0 \\ -e^{(-b_x(x-x_{beam})^2)}e^{(-b_y(y-y_{beam})^2)} \end{pmatrix} \ , \tag{2.15}$$

with boundary conditions $U(\bar{x}, \epsilon) = 0 \quad \forall \bar{x} \in \partial\Omega$. Physically this means, that the electrons start

traveling inside the specimen, but we can choose the position x_{beam}, y_{beam} close to the sample surface to make it realistic.

Congruity with the $\mathcal{M}1$-Model As the equations inside the domain (equation 2.1) also define the information flow over the boundary, our boundary conditions are not congruous to the model equations. Only the characteristics flowing into the domain should be set by boundary conditions. Our approach of modeling the beam as a boundary condition or setting the boundary to zero violates this condition. But if we request, that the computational domain Ω is large enough so electrons do not travel out of it, they work in practice (see section 2.3). Due to the large domain, the boundary has little effect on the solution.

It is also possible to extrapolate the solution at the boundary and obtain similar results, but all examples in this work use zero as a boundary condition.

2.1.4 $\mathcal{M}1$-Model as a Constraint to the Optimization Problem

The solution of the $\mathcal{M}1$-Model is dependent on beam position (x_{beam}, y_{beam}) and energy (ϵ_{beam}), which were previously defined by an experiment ex. With $\nabla_{\bar{x}} = \begin{pmatrix} \partial_x \\ \partial_y \end{pmatrix}$ and $F = \begin{pmatrix} F_x \\ F_y \end{pmatrix}$ we can denote the $\mathcal{M}1$-Model as

$$\begin{aligned} G_{ex}(U,p) = -\partial_\epsilon(S(\bar{x},\epsilon)U(\bar{x},\epsilon)) + \nabla_x F(U(\bar{x},\epsilon)) + T(\bar{x},\epsilon)U(\bar{x},\epsilon) = 0 \\ \forall \bar{x} \in \Omega, \epsilon \in [\epsilon_{cutoff}, \epsilon_{initial}] \ . \end{aligned} \tag{2.16}$$

If $G_{ex}(U_{ex}, p) = 0$, U_{ex} is a solution to the $\mathcal{M}1$-Model with parameters p and for an experiment ex. G_{ex} depends on the parameters p, because the material properties S and T depend on p. We can refer to G_{ex} as a constraint to the optimization problem defined in section 1.7

$$\begin{aligned} \min_p J(c) = \min_p \sum_{ex,i,j} \frac{1}{2}(k_{ex}^{i,j} - \tilde{k}_{ex}^{i,j})^2 \\ G_{ex}(U_{ex}, p) = 0 \quad \forall ex \ . \end{aligned} \tag{2.17}$$

Both equations are coupled, because the k-ratios $k_{ex}^{i,j}$ depend on the electron fluence, which is the first component of U_{ex}.

2.2 The Finite Volume Method in CLAWPACK

The $\mathcal{M}1$-Model, which was presented in the previous section, can be mathematically classified as a hyperbolic partial differential equation. A common method to solve hyperbolic equations are finite volume methods (FVM)[15][27]. In this section the theory of FVM is briefly presented and the implementation of the $\mathcal{M}1$-Model using the FV-framework CLAWPACK will be outlined.

In 1D finite volume methods are designed to solve problems of the type

$$\partial_t U(x,t) + \partial_x F(U(x,t)) = 0 \quad \forall x \in \Omega, t \in [0,T] \ , \tag{2.18}$$

where $U\colon \Omega \times [0,T] \to \mathbb{R}^n$ is the state variable, ∂_t and ∂_x denote the partial derivatives with respect to time and position and $F(\cdot)\colon \mathbb{R}^n \to \mathbb{R}^n$ is a flux function. An initial condition is given at time $t = 0$ by

$$U(x, t=0) = U_0(x) \quad \forall x \in \Omega \ . \tag{2.19}$$

As a spatial discretization, the domain Ω is divided into cells C_i with constant size Δx. The center point of each cell is x_i and the interfaces are at $x_{i\pm\frac{1}{2}}$. Finite volume methods only keep track of the solution by the mean value U_i of the solution $U(x,t)$ inside a grid cell C_i

$$U_i(t) = \frac{1}{\Delta x} \int_{C_i} U(x,t)\,\mathrm{d}x \ . \tag{2.20}$$

The time is discretized by time steps Δt, such that the numerical approximation is piece-wise constant in space for every time step

$$U^{num}(x,t) = \{U_i^n \text{ if } x \in C_i \text{ and } t \in [t^n, t^{n+1})\} \ . \tag{2.21}$$

The objective is to describe the evolution of the solution U regarding the jumps at cell interfaces, which are arising in the non-trivial case. This motivates the investigation of Riemann problems.

2.2.1 Riemann Problem

Consider the Riemann problem

$$\begin{aligned} \partial_t U(x,t) + \partial_x F(U(x,t)) &= 0 \qquad \forall x \in \Omega, t \in [0,T] \\ U(x, t=0) = U^0(x) &= \begin{cases} U_L & x \le x_0 \\ U_R & x > x_0 \end{cases} \ . \end{aligned} \tag{2.22}$$

The initial condition $U^0(x)$ consists of two states U_L and U_R, left and right of a given $x_0 \in \Omega$, hence there is a jump $\Delta U = U_R - U_L$ at x_0.

In the following various hyperbolic equations are considered, differentiated by their flux function F. The case of a linear scalar, a multivariable and a non-linear flux function are examined.

Linear Scalar For a linear scalar case, $U\colon \Omega\times[0,T]\to\mathbb{R}$, $n=1$, the flux function reads $F(U)=aU$ with $a\in\mathbb{R}$. The exact solution to this scalar advection problem is

$$U(x,t)=U^0(x-at)\ . \tag{2.23}$$

The jump ΔU is propagated through space with constant velocity a, meaning, that at time $\tilde{t}$ the jump is at $x_0+a\tilde{t}$ (see figure 5).

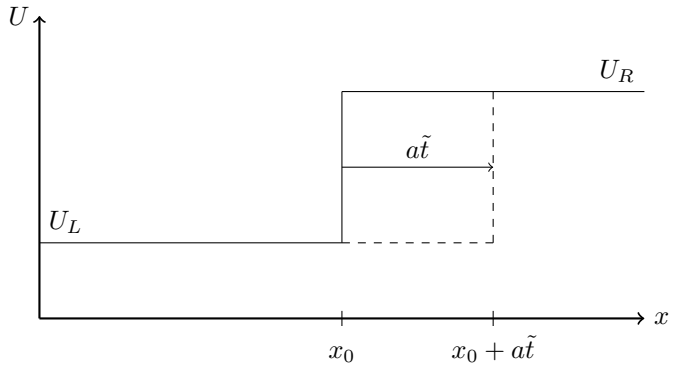

Figure 5: Linear scalar advection at $t=0$ and $t=\tilde{t}$

One can think of the jump ΔU as a wave, traveling through the solution.

Linear System For a linear system, $n\in\mathbb{N}$, the flux function is $F(U)=AU$, where $A\in\mathbb{R}^{n\times n}$ is a diagonalizable matrix with real eigenvalues $\Lambda=diag(\lambda_1,\lambda_2,\dots)$ and eigenvectors $T=(v_1,v_2,\dots)$.

Choosing characteristic variables $W(x,t)=T^{-1}U(x,t)$, equation (2.22) transforms to

$$\partial_t W(x,t)+\Lambda\partial_x W(x,t)=0\ . \tag{2.24}$$

While the original equations were coupled, the characteristic variables can be solved (as seen in the previous paragraph) independently as n scalar advection equations with initial conditions $W_0(x,t)=T^{-1}U_0(x,t)$. The velocities of the characteristic variables are the eigenvalues $\lambda_1,\lambda_2,\dots$ of A. The solution in characteristic variables then reads

$$W(x,t)=\begin{pmatrix}\vdots\\ w_i^0(x-\lambda_i t)\\ \vdots\end{pmatrix}\ . \tag{2.25}$$

The transformation back to the original variables is given by $U(x,t)=TW(x,t)$.

The initial jump ΔU in the solution U is split up and propagated. When splitting up the jump ΔU using the eigenvectors $\{v_1,v_2,\dots\}$

$$\sum_i \alpha_i v_i=\Delta U \qquad \alpha=T^{-1}\Delta U\ , \tag{2.26}$$

one can identify n waves, with height α_i and direction v_i.

Example To give an example of this behavior, choose

$$A = \begin{pmatrix} 1 & 1 & 0 \\ 0 & 2 & 0 \\ 0 & 0 & -1 \end{pmatrix} \quad U_L = \begin{pmatrix} 1 \\ 0.5 \\ 2.5 \end{pmatrix} \quad U_R = \begin{pmatrix} 3 \\ 1.5 \\ 1.5 \end{pmatrix} \quad x_0 = 0 \ . \tag{2.27}$$

The eigenvectors T and eigenvalues Λ of A as well as the wave heights α are

$$T = \begin{pmatrix} 1 & \sqrt{2}/2 & 0 \\ 0 & \sqrt{2}/2 & 0 \\ 0 & 0 & 1 \end{pmatrix} \quad \Lambda = \begin{pmatrix} 1 \\ 2 \\ -1 \end{pmatrix} \quad \alpha = \begin{pmatrix} 1 \\ \sqrt{2} \\ -1 \end{pmatrix} \ . \tag{2.28}$$

The positions of the waves are illustrated in the following figure 6. From the single discontinuity at $(x_0, t = 0)$ the three waves propagate with constant velocity λ_i such that at a later point in time t, the wave is at position $x_t = x_0 + \lambda_i t$.

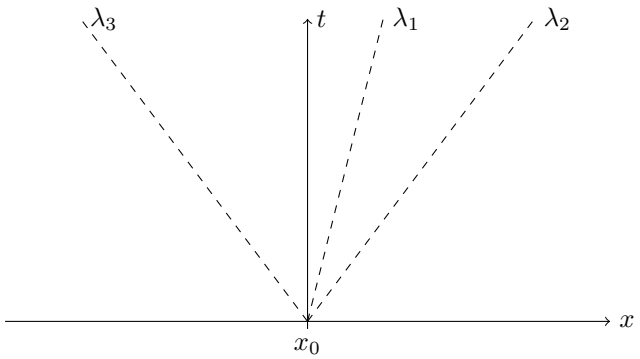

Figure 6: Propagation of waves originating from a single discontinuity

In figure 7 the solution of the specified linear Riemann problem is plotted at time $t = 0$ (solid line) and $t = 1$ (dashed line). When looking through the solution from left to right, one can identify the three waves and the states in between

$$U_L, \quad U_L + \alpha_3 v_3, \quad U_L + \alpha_3 v_3 + \alpha_1 v_1, \quad U_L + \alpha_3 v_3 + \alpha_1 v_1 + \alpha_2 v_2 = U_R \ . \tag{2.29}$$

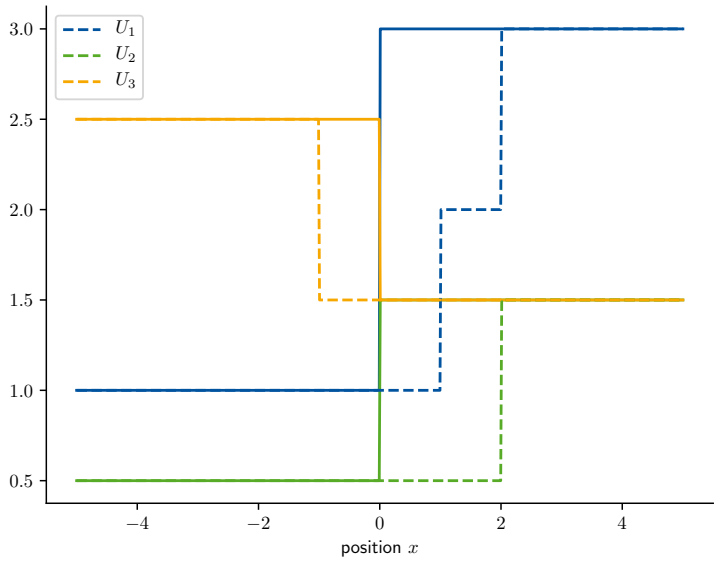

Figure 7: Plot of the solution at $t = 0$(solid) and $t = 1$(dashed)

Non-Linear System For an arbitrary flux function F we can write the Riemann problem, using the jacobian DF of F with respect to U, as follows:

$$\partial_t U(x,t) + DF(U(x,t))\partial_x U(x,t) = 0 \ . \tag{2.30}$$

In the linear system, the jacobian DF simply was the system matrix A and did not depend on U. In the non-linear case, the jacobian depends on U and therefore also its eigenvalues and eigenvectors. Because of the jump in ΔU it even is not clear where to evaluate DF.

If we find an approximation to the jacobian, the theory of linear systems can be applied, with the difficulty, that there is a different matrix for each Riemann problem. One possible approximation is the Roe matrix. A Roe matrix $\tilde{A}(U_L, U_R)$ fulfills the conditions to be

- diagonalizable with real eigenvalues,
- consistent: if $U_L, U_R \to U$ also $\tilde{A}(U_L, U_R) \to DF(U)$ and
- conserving: $\tilde{A}(U_L, U_R)(U_R - U_L) = F(U_R) - F(U_L)$.

Then the non-linear system can be treated similar to the linear system. Nevertheless it is difficult to construct such a matrix for arbitrary flux functions $F(U)$. In [15] the simplification $\tilde{A}(U_L, U_R) = DF(\frac{U_L+U_R}{2})$ is stated. Later I will use this approach in the numerical solution of the $\mathcal{M}1$-Model.

2.2.2 Wave Propagation Method

Now we want to extend the analysis of Riemann problems, to regard multiple jumps. Recall that finite volume methods keep track of the solution only by the mean value inside a grid cell U_i^n, so a jump cannot be described at an arbitrary position. From a given solution U_i^n at time t^n the goal is

to construct the solution U_i^{n+1} at t^{n+1}. The following description refers first to a linear problem, but the methods can later be extended to nonlinear ones.

Upwind Method for a Linear System Consider a cell C_i with its neighboring cells $C_{i\pm1}$ and their respective mean values U_i and $U_{i\pm1}$ with jumps at the two interfaces $\Delta U_{i\pm\frac{1}{2}}$ (cf. figure 8).

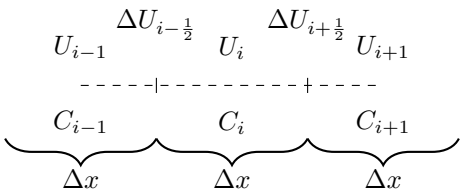

Figure 8: Three cells C_{i-1}, C_i, C_{i+1}

From each of the interfaces there are waves propagating into their neighboring cells. For reconstruction of U_i^{n+1} we only need to consider waves traveling into C_i, thus waves $W_{i-\frac{1}{2}}^{\lambda>0}$ originating from $\Delta U_{i-\frac{1}{2}}$ with positive wave speeds $\lambda_W > 0$ and waves $W_{i+\frac{1}{2}}^{\lambda<0}$ originating from $\Delta U_{i+\frac{1}{2}}$ with negative wave speeds $\lambda_W < 0$. At time $t^{n+1} = t^n + \Delta t$ the waves have propagated $\Delta t\lambda$ into cell C_i. The average value changed to

$$U_i^{n+1} = U_i^n - \sum_{W \in W_{i-\frac{1}{2}}^{\lambda>0}} \frac{\Delta t}{\Delta x} \lambda_W \alpha_W v_W - \sum_{W \in W_{i+\frac{1}{2}}^{\lambda<0}} \frac{\Delta t}{\Delta x} \lambda_W \alpha_W v_W \ , \tag{2.31}$$

where λ_W is the wave speed, $\alpha_W = T^{-1}\Delta U$ the wave height and v_W the wave's direction. With the introduction of A^+ and A^- as the recombination of an eigenvector T and eigenvalue Λ decomposition of A regarding only the positive Λ^+ /negative Λ^- eigenvalues

$$A^+ = T\Lambda^+T^{-1} = T \ \mathrm{diag}(\max(0, \lambda_i))T^{-1} \tag{2.32}$$

$$A^- = T\Lambda^-T^{-1} = T \ \mathrm{diag}(\min(0, \lambda_i))T^{-1} \ , \tag{2.33}$$

equation (2.31) can be written as

$$\begin{aligned} U_i^{n+1} &= U_i^n - \frac{\Delta t}{\Delta x} \left(\sum_{W \in W_{i-\frac{1}{2}}} \max(0, \lambda_W) \alpha_W v_W + \sum_{W \in W_{i+\frac{1}{2}}} \min(0, \lambda_W) \alpha_W v_W \right) \\ &= U_i^n - \frac{\Delta t}{\Delta x} \left(A^+ \Delta U_{i-\frac{1}{2}} + A^- \Delta U_{i+\frac{1}{2}} \right) \\ &= U_i^n - \frac{\Delta t}{\Delta x} \left(A^+ \left(U_i^n - U_{i-1}^n \right) + A^- \left(U_{i+1}^n - U_i^n \right) \right) \ . \end{aligned} \tag{2.34}$$

This method (equation(2.34)) is called upwind method for a linear system, because eg. for a wave moving to the right (positive eigenvalue), the left jump is used for approximation of $\partial_x U$.

Another common notation for finite volume methods is

$$U_i^{n+1} = U_i^n + \frac{\Delta t}{\Delta x} (\tilde{F}_{i-\frac{1}{2}} - \tilde{F}_{i+\frac{1}{2}}) \ , \tag{2.35}$$

where $\tilde{F}_{i\pm\frac{1}{2}}$ is the numerical flux which has to be reconstructed from the two states of U surrounding

the interface $i \pm \frac{1}{2}$. The numerical flux function for the upwind method is[15][27]

$$\tilde{F}_{i-\frac{1}{2}} = A^+ U^n_{i-1} + A^- U^n_i \tag{2.36}$$

$$\tilde{F}_{i+\frac{1}{2}} = A^+ U^n_i + A^- U^n_{i+1} \ , \tag{2.37}$$

which is the flux function evaluated at an interim state $U^*_{i\pm\frac{1}{2}}$

$$\tilde{F}_{i-\frac{1}{2}} = F(U^*_{i-\frac{1}{2}}) \ . \tag{2.38}$$

The interim state $U^*_{i\pm\frac{1}{2}}$ is the state of the solution at $x_{i\pm\frac{1}{2}}$ directly after t^n. It can be constructed using the eigenvectors and eigenvalues

$$U^*_{i+\frac{1}{2}} = U^n_i + \sum_{W \in W^{\lambda<0}_{i+\frac{1}{2}}} \alpha_W v_W = U^n_{i+1} - \sum_{W \in W^{\lambda>0}_{i+\frac{1}{2}}} \alpha_W v_W \tag{2.39}$$

$$U^*_{i-\frac{1}{2}} = U^n_{i-1} + \sum_{W \in W^{\lambda<0}_{i-\frac{1}{2}}} \alpha_W v_W = U^n_i - \sum_{W \in W^{\lambda>0}_{i-\frac{1}{2}}} \alpha_W v_W \ . \tag{2.40}$$

Lax Wendroff Method The upwind method is first order accurate[15]. A method of second order is the Lax Wendroff Method. If we write equation (2.18) as

$$\partial_t U = -A \partial_x U \ , \tag{2.41}$$

the second partial derivative with respect to time can be deduced

$$\partial_{tt} U = \partial_t(-A\partial_x U) = A^2 \partial_{xx} U \ . \tag{2.42}$$

The Taylor series in time of the solution U at a point x is

$$U(x, t+\Delta t) = U(x,t) + \Delta t \partial_t U(x,t) + \frac{\Delta t^2}{2} \partial_{tt} U(x,t) + \mathcal{O}(\Delta t^3) \ , \tag{2.43}$$

which is, by replacing temporal with spatial derivatives (2.41) and (2.42)

$$U(x, t+\Delta t) = U(x,t) - \Delta t A \partial_x U(x,t) + \frac{\Delta t^2}{2} A^2 \partial_{xx} U(x,t) \ . \tag{2.44}$$

Using finite difference approximations for the spatial derivatives of U, this can be written as

$$U^{n+1}_i = U^n_i - \frac{\Delta t}{2\Delta x} A (U^n_{i+1} - U^n_{i-1}) + \frac{\Delta t^2}{2\Delta x^2} A^2 (U^n_{i-1} - 2U^n_i + U^n_{i+1}) \ . \tag{2.45}$$

Although the derivation is based on a finite difference scheme, the Lax Wendroff Method can be written in conservative finite volume form [15]

$$U^{n+1}_i = U^n_i + \frac{\Delta t}{\Delta x} (\tilde{F}_{i-\frac{1}{2}} - \tilde{F}_{i+\frac{1}{2}}) \ , \tag{2.46}$$

together with the numerical flux

$$\tilde{F}_{i-\frac{1}{2}} = \frac{1}{2}A(U^n_{i-1} + U^n_i) - \frac{\Delta t}{2\Delta x}A^2(U^n_i - U^n_{i-1}) \ . \tag{2.47}$$

The numerical flux $\tilde{F}_{i+\frac{1}{2}}$ can be derived from equation (2.47) by changing $i \to i+1$. Since in the Taylor series terms higher than order 2 got omitted, the Lax Wendroff Method is second order accurate.

Limiters It is known, that second order schemes tend to oscillate around discontinuities [8] [15]. To maintain second order accuracy in smooth regions of the solution and prevent oscillations around discontinuities, there is the concept of flux limiting.

If we, asides from A^+ and A^-, define $|A| = A^+ - A^-$ the "absolute value" of $A = A^+ + A^-$, it can be proved that $A^2 = |A|^2$. The Lax Wendroff flux (equation (2.47)) can be, using the binomial formula and the previously derived properties of $|A|$, written as

$$\tilde{F}_{i-\frac{1}{2}} = A^+U^n_{i-1} + A^-U^n_i + \frac{1}{2}|A|(I - \frac{\Delta t}{\Delta x}|A|)(U^n_i - U^n_{i-1}) \ . \tag{2.48}$$

The first two summands are the same as in the flux for the upwind method (2.36). The upwind method is first order accurate, so we can interpret the last summand as second order correction terms. One can also split up the correction term and write a correction for each independent wave

$$\tilde{F}_{i-\frac{1}{2}} = A^+U^n_{i-1} + A^-U^n_i + \frac{1}{2}\sum_{W \in W_{i-\frac{1}{2}}} |\lambda_W|\,(1 - \frac{\Delta t}{\Delta x}\,|\lambda_W|)\alpha_W v_W \ . \tag{2.49}$$

To reduce the order of accuracy of the flux to first order at discontinuities, a limiter variable Φ is introduced. The idea is to limit each wave independently

$$\tilde{F}_{i-\frac{1}{2}} = A^+U^n_{i-1} + A^-U^n_i + \frac{1}{2}\sum_{W \in W_{i-\frac{1}{2}}} |\lambda_W|\,(1 - \frac{\Delta t}{\Delta x}\,|\lambda_W|)\Phi_W\alpha_W v_W \ . \tag{2.50}$$

If $\Phi_W = 0$ the correction term for the wave W vanishes and the flux is first order accurate, otherwise if $\Phi = 1$ the second order accuracy is retained.

Φ_W should depend on a measure of discontinuity of each wave $W \in W_{i-\frac{1}{2}}$, therefore we introduce

$$\theta_W = \frac{\alpha_V}{\alpha_W} \qquad V \in W_{I-\frac{1}{2}} \quad I = \begin{cases} i-1 & \lambda_W > 0 \\ i+1 & \lambda_W < 0 \end{cases} \ . \tag{2.51}$$

V is the wave of the same family as W, meaning they both arise from the same eigenvalue/vector, but from the neighboring interface $I - \frac{1}{2}$. The direction of travel decides whether to take the right or left $i \pm 1 - \frac{1}{2}$ neighboring interface.

There are many different functions for $\Phi(\theta)$, two commonly used limiters are

- **minmod:** $\Phi(\theta) = \max(0, \min(1, \theta))$ and
- **superbee:** $\Phi(\theta) = \max(0, \min(2\theta, 1), \min(\theta, 2))$.

CFL Condition Waves from an interface may only affect their neighboring cells. So the time step has to be chosen such that

$$\Delta t \leq \frac{\Delta x}{|\lambda|} \ , \tag{2.52}$$

where $|\lambda|$ is the maximum wave speed in the solution[15] [27]. From this we can derive the CFL condition that must be met for each time step

$$\text{CFL} = \frac{|\lambda|\Delta t}{\Delta x} \leq 1 \ . \tag{2.53}$$

This means that Δt and Δx cannot be chosen independently of each other.

Extension to Non-Linear Systems The wave propagation method has been described for a linear system, but it can be extended to non-linear systems [15]. As the jacobian then depends on U, it has to be approximated (eg. with a Roe matrix) and different waves λ_W, α_W have to be calculated for each interface. Then the second order update for each cell can be done using the equation (2.35) with the flux function (2.51).

2.2.3 2D Implementation in CLAWPACK

The FVM framework CLAWPACK[17] implements the previously presented method. In this section I comment on the implementation of CLAWPACK and my implementation of the $\mathcal{M}1$-Model with CLAWPACK.

CLAWPACK Implementation of FVM In its 2D Version the finite volume library CLAWPACK [5] [15] [17] solves equations of the form

$$\kappa(x,y,t)\partial_t U(x,y,t) + \partial_x F_x(U(x,y,t)) + \partial_y F_y(U(x,y,t)) = \psi(x,y,t) \tag{2.54}$$

with an initial condition

$$U(x,y,t=0) = U_0(x,y) \ . \tag{2.55}$$

CLAWPACK uses a splitting approach and first solves the x-direction $\partial_x F_x(U)$, then the y-direction $\partial_y F_y(U)$ and finally the source term ψ, which can also depend on U. The capacity coefficient κ can be specified before each time step. The wave propagation method described above is used with first or second order accuracy, together with a limiter function.

To implement a custom problem, one has to define

- **the discretization and simulation properties**: the computational domain, number of grid cells, end time, desired CFL number, etc.,
- **a Riemann solver**: a function returning the waves, wave speeds and "fluctuations" $A^{\pm}\Delta U$, for a 1D slices through the solution in x/y-direction,
- **a before-step function**,which sets the capacity coefficient, and precalculates other properties used in the Riemann solver or the source function and
- **a source function**, which given a solution U and a time step dt this function integrates the source term and adds it to the solution.

$\mathcal{M}1$-Model Implementation Now the $\mathcal{M}1$-Model is to be tailored, such that it fits the CLAWPACK form (equation (2.54)). The $\mathcal{M}1$-Model has the following structure

$$-\partial_\epsilon(S(\bar{x},\epsilon)U(\bar{x},\epsilon)) + \partial_x F_x(U(\bar{x},\epsilon)) + \partial_y F_y(U(\bar{x},\epsilon)) = -T(\bar{x},\epsilon)U(\bar{x},\epsilon)\ . \tag{2.56}$$

The energy ϵ is transformed to a pseudo time variable t, as it acts like the temporal derivative in equation (2.54)

$$t(\epsilon) = \epsilon_{initial} - \epsilon \tag{2.57}$$

$$\epsilon(t) = \epsilon_{initial} - t\ . \tag{2.58}$$

Then the derivative reads

$$\partial_\epsilon f(t(\epsilon)) = \partial_t f(t)\frac{d\epsilon(t)}{dt} = -\partial_t f(t) \tag{2.59}$$

and the pseudo time domain is

$$t \in [t(\epsilon_{initial}), t(\epsilon_{cutoff})] = [0, T]\ . \tag{2.60}$$

Using the chain rule and the pseudo-time transformation, equation (2.56) can be written in the CLAWPACK conform way

$$S(\bar{x},t)\partial_t U(\bar{x},t) + \partial_x F_x(U(\bar{x},t)) + \partial_y F_y(U(\bar{x},t)) = (T(\bar{x},t) - \partial_t S(\bar{x},t))U(\bar{x},t)\ . \tag{2.61}$$

Comparison with the CLAWPACK model equation (2.54) yields

- $S = \kappa$ the stopping power as the capacity coefficient and
- $(T - \partial_t S)U = \psi$ as the source term.

To implement a Riemann solver for CLAWPACK the eigenvalues and eigenvectors of the jacobian of the flux functions F_x and F_y are required. The jacobian matrices are derived for a 2D System in [18]. The eigensystem decomposition as well as the inversion of the eigenvector matrix is done numerically using the Linear Algebra PACKage (LAPACK)[1] in FORTRAN.

2.3 Evaluation of the $\mathcal{M}1$-Model

The previously developed method is used to exemplary simulate the interaction of electrons in an sample of nickel ($Z = 28$, $A = 58.6934\frac{\mathrm{g}}{\mathrm{mol}}$) and chromium ($Z = 24$, $A = 51.9961\frac{\mathrm{g}}{\mathrm{mol}}$). The electron beam has an energy of $\epsilon_{beam} = 12$ keV and hits the specimen on the upper boundary at position $x_{beam} = 0$. The computational domain has the dimensions $[-500\ \mathrm{nm}, 500\ \mathrm{nm}] \times [-700\ \mathrm{nm}, 0\ \mathrm{nm}]$ discretized by a 50×50 grid and the detector is in the origin $(0\ \mathrm{nm}, 0\ \mathrm{nm})$. The electrons are simulated in a range from $\epsilon_{initial} = 13$ keV to $\epsilon_{cutoff} = 5.2$ keV. CLAWPACK is set up to use its second order reconstruction.

The material is vertically divided in the middle. In the left and right part, the mass concentrations are

$$c_{Ni,l} = 0.2 \quad c_{Ch,l} = 0.8 \qquad c_{Ni,r} = 0.8 \quad c_{Ch,r} = 0.2\ . \tag{2.62}$$

The density $\rho = 8.96 \times 10^3\,\frac{kg}{m^3}$ is constant in the whole material.

In figure 9 the electron fluence u_1 is plotted for multiple energies. While the high energy electrons are concentrated near the point of beam exposure, lower energy electrons are diffused deeper in the sample. If the right and left sides are examined closely, the effects of the different mass concentrations can be identified. Chromium has a lower stopping power and also a lower transport coefficient than nickel, therefore the electrons penetrate slightly deeper on the left side.

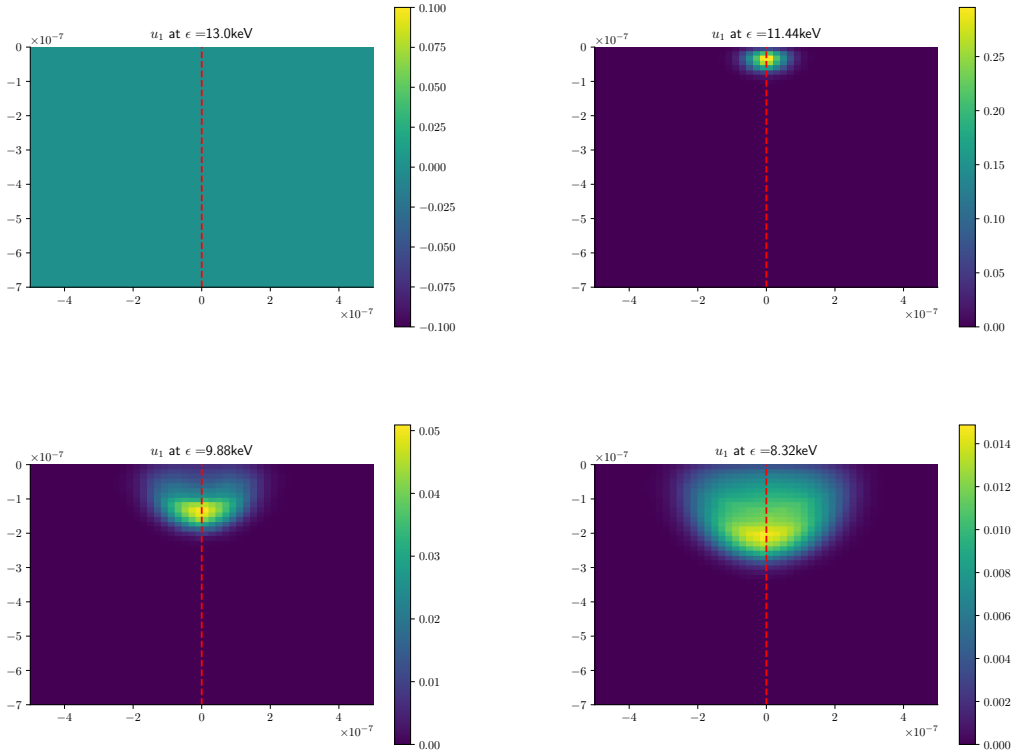

Figure 9: The electron fluence at different energies

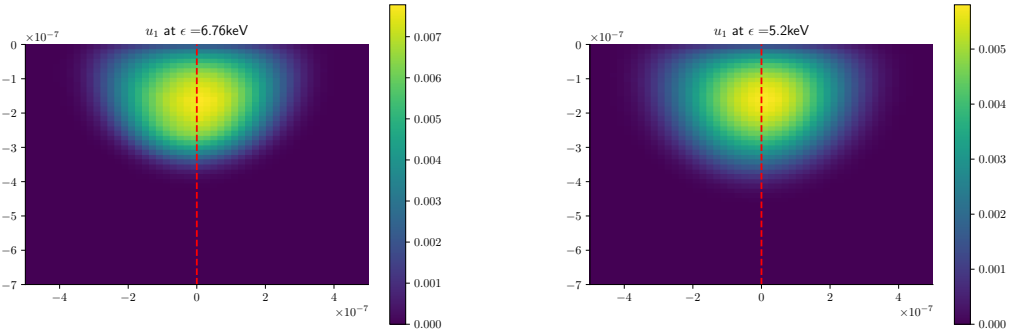

Figure 9 (cont.): The electron fluence at different energies

With the electron fluence we can, as explained in section 2.1, calculate an effective intensity of generated x-rays for every grid cell. These are shown in figure 10 for the $K\alpha$ x-rays of nickel and

chromium. The attenuation is already included in these pictures. Here the separation in left and right mass concentrations emerges more clearly.

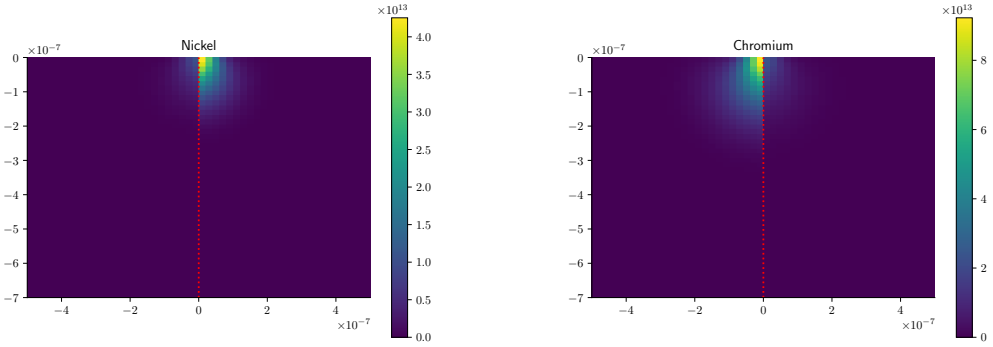

Figure 10: Characteristic x-ray intensities of nickel and chromium

It is important to choose the energy steps of the finite volume method around the beam energy small enough, such that the electron beam is captured sufficiently. In figure 11 the energy steps are plotted onto the beam intensity.

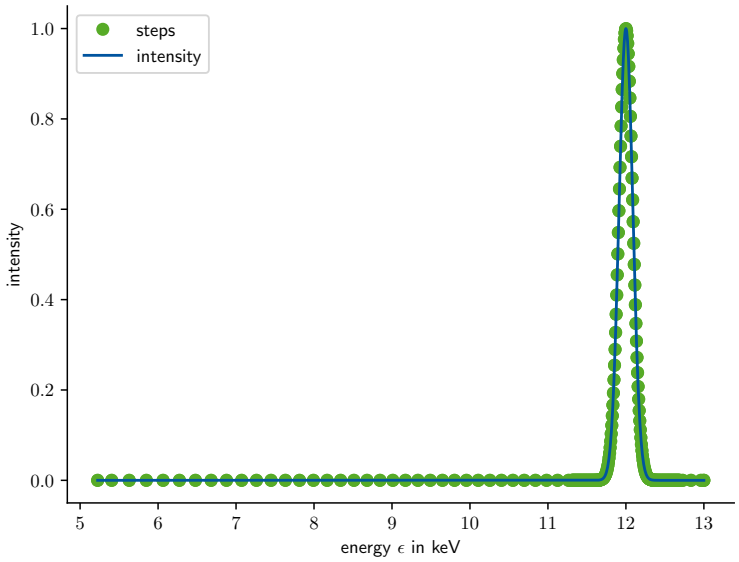

Figure 11: Plot of the FV energy steps and the beam intensity

When choosing a standard intensity $I_{std} = 1{\times}10^{-27}$ to scale the k-ratios, the simulation yields

$$k^{Ni} = 0.25 \quad \text{and} \quad k^{Ch} = 1.2\ . \tag{2.63}$$

From a given set of mass concentrations and densities we are able to calculate the k-ratios for different elements. But the goal is to solve the inverse problem, to reconstruct mass concentrations

and density from given k-ratios. In the following section 3 we will use this model to solve the inverse problem.

3 Solving the Inverse Problem

In section 1 the calculation of k-ratios $k^{i,j}$ from the electron fluence $\psi^0(\bar{x}, \epsilon)$ was derived. In section 2 the $\mathcal{M}1$-Model was detailed to calculate the electron fluence $\psi^0(\bar{x}, \epsilon)$. This section deals with solving the inverse problem using gradient based optimization methods. Those methods are best suited for convex functions, therefore our objective function J should be convex at least in an interval around its minimum.

Recall that the inverse problem (equation (3.1)) introduced in section 1.7 and extended by a constraint in section 2.1.4 reads

$$\begin{aligned} \min_p J(c) = \min_p \sum_{ex,i,j} \frac{1}{2}(k_{ex}^{i,j} - \tilde{k}_{ex}^{i,j})^2 \\ G_{ex}(U_{ex}, p) = 0 \quad \forall ex \ . \end{aligned} \tag{3.1}$$

In this section the objective function J is analyzed, then gradient based methods to solve optimization problems are presented and finally a fast and accurate way to calculate the gradient of the objective function using the adjoint state method is presented.

3.1 Analysis of the Objective Function

To get an idea of the behavior of the objective function, several numerical experiments with differently characterized mass concentration in the domain Ω were performed.

Homogeneous Mass Concentration The considered sample consists of nickel and chromium with a homogeneous mass concentration c_{Ni} and c_{Cr} in the whole domain Ω. Other settings are chosen according to section 2.3. Recall that the concentrations always have to add to one, so for two elements one variable is sufficient (section 1.1).

The measured k-ratios $\tilde{k}_{ex}^{i,j}$ were simulated using concentrations of $\tilde{c}_{Ni} = \tilde{p} = 0.5$ and $\tilde{c}_{Cr} = 1 - \tilde{p} = 0.5$, therefore the minimum of the objective function is at $p = 0.5$. In figure 12 the plot shows the objective function for a range of parameters $p \in [0, 1]$.

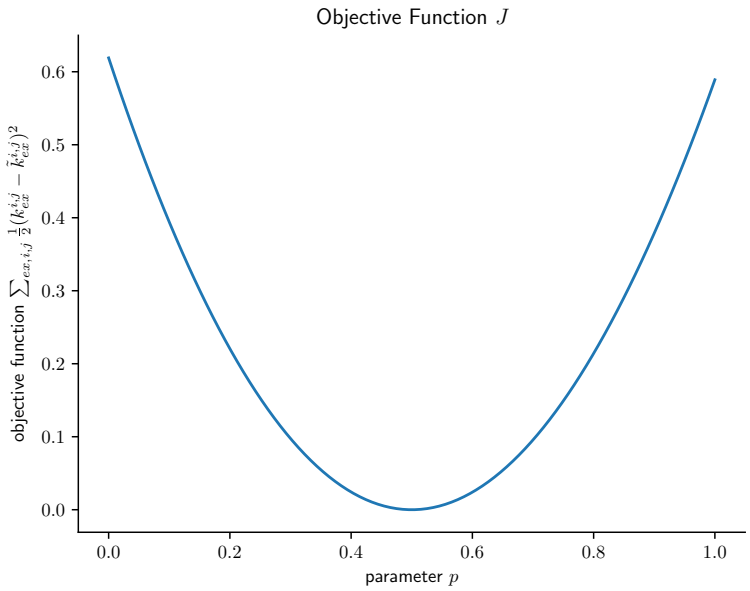

Figure 12: Objective function for a homogeneous material of nickel and chromium

Left and Right Mass Concentrations In the second example the sample is, as in section 2.3, vertically divided. We need two parameters describing the left p_l and the right p_r mass concentrations.

For a single electron bombardment at the center $x_{beam} = 0$, the objective function does not provide a unique minimum. Since the detector is at position $(0\text{ nm}, 0\text{ nm})$ and cannot measure the origin of detected x-rays, the problem is symmetric, meaning that the k-ratios are the same for p_l, p_r and $\hat{p_l} = p_r, \hat{p_r} = p_l$. In 2.3 k-ratios for $p_l = 0.2$ and $p_r = 0.8$ were calculated. If we set $p_l = 0.8$ and $p_r = 0.2$ exactly the same k-ratios are obtained. They are also very similar when concentrations are chosen such that the mean concentration $\frac{p_l + p_r}{2}$ matches the mean concentration of the reference.

To account for those problems, two different experiments with different beam positions are used. One where the beam position was set left to the detector $x_{beam} = -100$ nm and one where $x_{beam} = 100$ nm. In doing so the objective function provides a unique minimum for the reference parameters $\tilde{p_l} = 0.8$ and $\tilde{p_r} = 0.4$, shown in figure 13. For $p_l = 0.4$ and $p_r = 0.8$ no minimum is visible, consequently the problem with symmetry is solved with two beam positions.

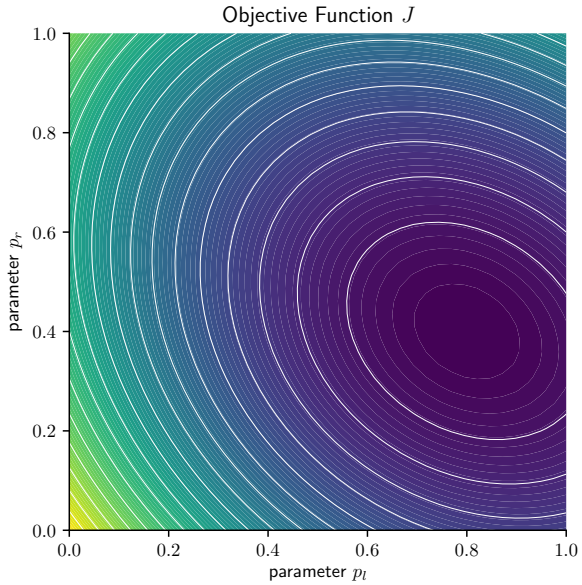

Figure 13: Objective function for a vertically divided material of nickel and chromium

Mass Concentrations defined on a Small Grid Another point of interest is the question whether it is possible to resolve the mass concentrations on a scale smaller then the size of the interaction volume. Therefore the domain is vertically and horizontally divided in 10 grid cells and four parameters p_0, p_1, p_2 and p_3 are chosen which describe the mass concentrations of nickel and chromium in four cells inside the domain. Two beam positions, -100nm and 100nm as well as two beam energies, 8keV and 15keV were used. This setup is sketched in figure 14, where the four cells, the two beam positions and the impact zones of the electrons for both beam energies are shown.

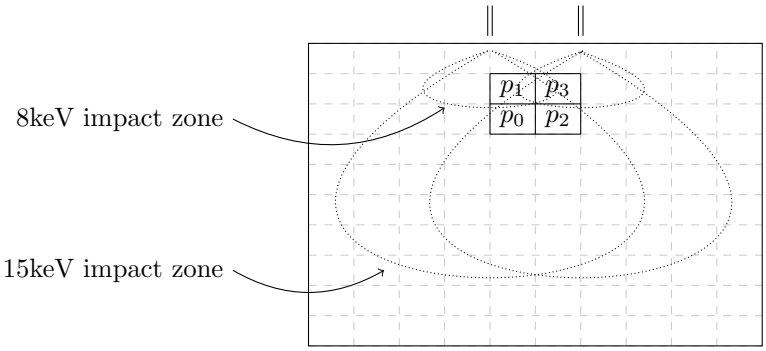

Figure 14: Four variable cells, the positions of the beam and the impact zones of the electrons

The measured k-ratios $\tilde{k}_{ex}^{i,j}$ were calculated with the parameters set to $\tilde{p} = (0.4, 0.6, 0.7, 0.2)^T$. In figure 15 the objective function is plotted for variable concentrations p_0 and p_2. You can see that the cells can partially balance each other out, so that if e.g. p_0 contains less and p_2 contains more nickel, the target function remains small. But a minimum is clearly visible at $p_0 = 0.4, p_2 = 0.7$.

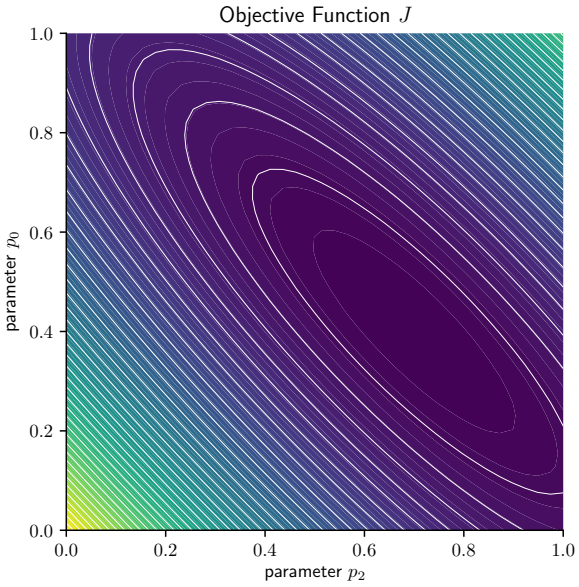

Figure 15: Objective function varying p_0 and p_2

For two cells p_0 and p_1 lying below each other, it is more challenging to visualize a minimum. To reach the lower cell p_0 the electrons always have to travel through the upper cell p_1, therefore changes in p_1 have a much stronger effect on the target function. By different weighting of the target function of the two experiments with 8keV and 15keV a minimum is visible here

$$J(p) = J_{15\text{keV}}(p) + 1000 J_{8\text{keV}}(p) \ . \tag{3.2}$$

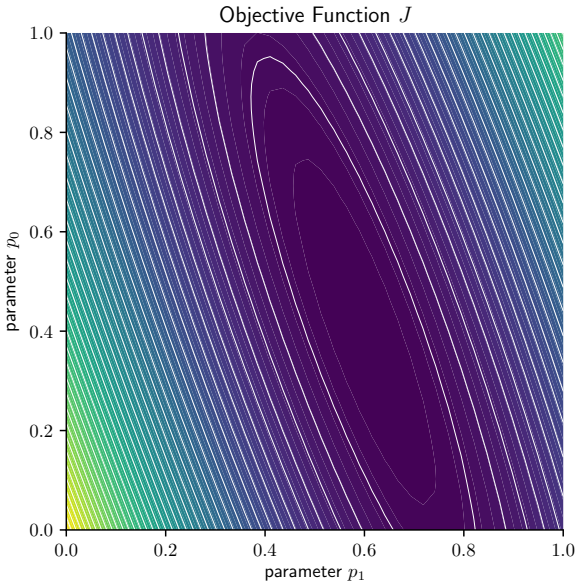

Figure 16: Objective function varying p_0 and p_1

Figure 16 shows the weighted objective function for variable concentrations p_0 and p_1.

It is not possible to visualize the objective function and vary all four parameters. But it can be checked whether the hessian of the objective function is positive definite at the reference values, which yields at least a local minimum. The eigenvalues of the hessian at the minimum $p = (0.4, 0.6, 0.7, 0.2)^T$ are

$$\lambda_0 = 7.25 \times 10^{-3} \quad \lambda_1 = 6.70 \times 10^{-4} \quad \lambda_2 = 4.74 \times 10^{-6} \quad \lambda_3 = 5.62 \times 10^{-7} \tag{3.3}$$

and are all greater than zero, therefore the hessian is positive definite.

Difficulties with the density When varying the density ρ only very small variation in the objective function is visible. After investigating the dependence of the density in the $\mathcal{M}1$-Model equations, we found that the stopping power and the transport coefficient depend linearly on the density ρ, therefore division by ρ introduces $\frac{1}{\rho}$ in the flux term. That means that for a homogeneous density $\rho(x) = \rho_{const}$, only the "velocities of the waves" (section 2.2) get scaled and simultaneously the impact zone of the electron inside the material. For a higher density, the electrons lose energy faster and the impact zone shrinks.

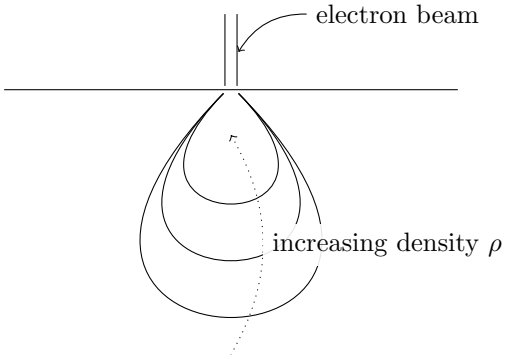

Figure 17: Impact zone of the electrons for different densities

If we think of the k-ratios as an integral over the electron fluence, a variation in the density cannot be seen in the objective function. Although the $\mathcal{M}1$-Model distinguishes between different densities (the electron fluence varies), the detector cannot measure this difference, as it detects all generated x-rays. Therefore it is not possible to reconstruct the density with our method and all future analysis in this work will only concern mass concentrations.

3.2 Optimization

In the previous section the expected minimum was known and the objective function was observed in order to find out whether this minimum is locatable. Now it is assumed, that the actual minimum is unknown and should be reconstructed by minimization of the objective function.

3.2.1 Gradient Based Optimization

To solve an optimization problem there are a range of methods based on a simple iterative scheme. Given an initial estimate p_0, the parameters p are updated using

$$p_{k+1} = p_k + \alpha_k \Delta p_k \tag{3.4}$$

until the objective function $J(p_k)$ does not decrease further, such that a minimum can be considered. Two common examples are

the steepest descend method $\Delta p_k = -\nabla_p J(p_k)$ and

the conjugate gradient method $\Delta p_k = -\nabla_p J(p_k) + \beta_k \Delta p_{k-1}$,

where α_k and β_k are step sizes. Both methods exploit the gradient of the objective function $\nabla_p J(p_k)$ with respect to p to find the increment Δp_k[20]. There is a variety of more sophisticated optimization methods to solve this problem, but many of them require the gradient of the objective function. In this work, the optimization function of the Python package SciPy [13] is used, which acts like a wrapper to the optimization methods implemented in SciPy. The methods the user has to define are

- the objective function,
- the gradient of the objective function and
- the initial parameters.

The method then chooses which optimization algorithm to use. But we still need to serve the gradient of the objective function.

3.2.2 Gradient of the Objective Function

As the objective function J is a sum of the experiment specific objective function

$$J(p) = \sum_{ex} J_{ex}(p) \ , \tag{3.5}$$

also the gradient of the objective function can be written as a sum of

$$\nabla_p J(p) = \sum_{ex} \nabla_p J_{ex}(p) \ . \tag{3.6}$$

This means that it is sufficient to find an expression for the experiment specific gradient $\nabla_p J_{ex}(p)$, which can be calculated independently. Therefore all quantities in the following sections refer to one specific experiment.

3.2.3 Finite Difference Approximation

We can aproximate the gradient using a finite difference approximation. The gradient with respect to p contains the derivatives of the objective functional $J(p)$ with respect to every element of p. Recall that the parameters p in our problem are the material parameters in each cell we want to

reconstruct. A finite difference approximation can be written as

$$\partial_{p_k} J(p) = \frac{J(p + he_k) - J(p)}{h} \quad h << 1 \ , \tag{3.7}$$

where h has to be chosen small enough to achieve sufficient accuracy. This has to be evaluated for every parameter dimension, and therefore the objective function together with the constraint has to be computed. Evaluating the constraint means solving a PDE system, which is expensive. Another method to calculate the gradient is preferrable.

3.2.4 Adjoint Gradient Calculation

An alternative to calculate the gradient is the adjoint state method. It is in no sense restricted to the inverse problem considered in this work. With many uses in geophyics and engineering it is often used as a faster alternative to finite differences. In [7] this method is used in aerodynamic shape optimization where the goal was to construct a aircraft wing shape such that the drag, the lift and the pitching moment are optimized. In seismic analysis the adjoint state method is used [20] [22] to discover the structure of the sea floor.

In this section the derivation of this method is described using a generalized objective function

$$J(p) = h(U_p, p) \ , \tag{3.8}$$

where the objective functional $h(U_p, p) = J(p)$ demonstrates the dependency of the objective function from the state variable U_p, the solution of $G(U_p, p) = 0$.

The goal is to calculate the gradient of the objective function $\frac{\partial J(p)}{\partial p}$. With h we can write

$$\frac{\partial J(p)}{\partial p} = \langle \frac{\delta h(U_p, p)}{\delta u}, \frac{\partial U_p}{\partial p} \rangle + \frac{\partial h(U_p, p)}{\partial p} \ . \tag{3.9}$$

In a discrete evaluation, the derivative $\frac{\partial U_p}{\partial p}$ would mean, to differentiate every discrete grid value with respect to every parameter. Especially with a high number of parameters this calculation is computationally intensive, but can be avoided using the adjoint state method.

For its derivation the adjoint operator and the functional derivative are of importance. The adjoint operator T^* allows us to isolate variables in the scalar product[28]

$$\langle Tx, y \rangle = \langle x, T^* y \rangle \ . \tag{3.10}$$

The functional derivative $\frac{\delta F(U)}{\delta U}$ is a generalization of the derivative for functionals[28].

Derivation from the Lagrange Functional The Lagrange functional in constrained optimization reads

$$L\left(U, \lambda, p\right) = h\left(U, p\right) - \langle \lambda, G\left(U, p\right) \rangle \ , \tag{3.11}$$

where λ is referred to as the adjoint state variable. If U solves the PDE-constraint $G(U, p) = 0$ we can conclude $U = U_p$ and the Lagrange functional coincides with the objective function $J(p)$

$$L\left(U_p, \lambda, p\right) = h\left(U_p, p\right) - \langle \lambda, \underbrace{F\left(U_p, p\right)}_{=0} \rangle = h\left(U_p, p\right) = J\left(p\right) \ . \tag{3.12}$$

Since equation (3.12) holds for every parameter p if $U = U_p$, the gradient of the Lagrange functional also coincides with the gradient of the objective function

$$\frac{dL(U_p, \lambda, p)}{dp} = \frac{\partial J(p)}{\partial p} \ . \tag{3.13}$$

To derive $\frac{dL(U_p,\lambda,p)}{dp}$, L is perturbed with δp_k, a small change in the k-th parameter. U_p is related to p through $G(U_p, p) = 0$, hence the perturbation δp_k causes a perturbation in $\delta U_p = \frac{\partial U_p}{\partial p_k}\delta p_k$. Inserting $U_p + \delta U_p$ and $p + \delta p_k$ into the Lagrange functional yields

$$\begin{aligned}
&L\left(U_p + \delta U_p, \lambda, p + \delta p_k\right) \\
&= h\left(U_p + \delta U_p, p + \delta p_k\right) - \langle \lambda, G\left(U_p + \delta U_p, p + \delta p_k\right)\rangle \\
&\approx h\left(U_p, p\right) + \langle \frac{\delta h\left(U_p, p\right)}{\delta U}, \delta U_p\rangle + \langle \frac{\partial h\left(U_p, p\right)}{\partial p_k}, \delta p_k\rangle \\
&\qquad\qquad - \langle \lambda, G\left(U_p, p\right) + \frac{\partial G\left(U_p, p\right)}{\partial U}\delta U_p + \frac{\partial G\left(U_p, p\right)}{\partial p_k}\delta p_k\rangle \\
&= L\left(U_p, \lambda, p\right) + \underbrace{\langle \frac{\delta h\left(U_p, p\right)}{\delta U}, \delta U_p\rangle - \langle \lambda, \frac{\partial G\left(U_p, p\right)}{\partial U}\delta U_p\rangle}_{\langle \frac{\delta L\left(U_p,\lambda,p\right)}{\delta U}, \delta U_p\rangle} \\
&\qquad\qquad + \underbrace{\langle \frac{\partial h\left(U_p, p\right)}{\partial p_k}, \delta p_k\rangle - \langle \lambda, \frac{\partial G\left(U_p, p\right)}{\partial p_k}\delta p_k\rangle}_{\langle \frac{\partial L\left(U_p,\lambda,p\right)}{\partial p_k}, \delta p_k\rangle} \ .
\end{aligned} \tag{3.14}$$

The perturbation $\delta U_p = \frac{\partial U_p}{\partial p}\delta p_k$ still contains the expensive term $\frac{\partial U_p}{\partial_p}$, but if λ is chosen such that

$$\frac{\delta L\left(U_p, \lambda, p\right)}{\delta U} = 0 \ , \tag{3.15}$$

the first scalar product of equation (3.14), $\langle \frac{\delta L(U_p,\lambda,p)}{\delta U}, \delta U_p\rangle = 0$ and the gradient of the objective function would simplify to

$$\frac{\partial J(p)}{\partial p_k} = \frac{\partial L(U_p, \lambda, p)}{\partial p_k} \ . \tag{3.16}$$

With equation (3.15) λ is chosen such that at U_p the derivative of the Lagrange functional with respect to U is zero. This means the Lagrange functional does not change locally if U changes, so the derivative of the Lagrange functional with respect to the parameter p, where usually the perturbation in U_p has to be considered, can be written as equation (3.16). The three main steps to calculate the gradient of the objective function then are

- solving the forward equation $G(U_p, p) = 0$ for U_p,
- solving the adjoint equation (equation (3.15)) for λ and
- calculating the scalar product for $\nabla_p J(p)$.

Solving the forward equation for U_p To obtain the physical solution U_p for parameters p, the PDE constraint has to be solved for U_p

$$G(U_p, p) = 0 \ . \tag{3.17}$$

Solving the adjoint equation for λ In equation (3.14) the relation

$$\langle \frac{\delta L\left(U_p, \lambda, p\right)}{\delta U}, \delta U_p \rangle = \langle \frac{\delta h\left(U_p, p\right)}{\delta U}, \delta U_p \rangle - \langle \lambda, \frac{\partial G\left(U_p, p\right)}{\partial U} \delta U_p \rangle \tag{3.18}$$

was found. Using the adjoint operator $\frac{\partial G(U_p,p)}{\partial U}^*$ the functional derivative of the Lagrange functional L can be written as

$$\frac{\delta L\left(U_p, \lambda, p\right)}{\delta U} = \frac{\delta h\left(U_p, p\right)}{\delta U} - \frac{\partial G\left(U_p, p\right)}{\partial U}^* \lambda = 0 \ . \tag{3.19}$$

Finding the adjoint operator $\frac{\partial G}{\partial U}^*$ involves boundary integrals, which have to be considered carefully. A detailed example is given in the derivation of these equations for the $\mathcal{M}1$-Model in section 3.3.

Solving the scalar product for $\nabla_p J(p)$ In equation (3.14) also the following relation was derived

$$\langle \frac{\partial L\left(U_p, \lambda, p\right)}{\partial p_k}, \delta p_k \rangle = \langle \frac{\partial h\left(U_p, p\right)}{\partial p_k}, \delta p_k \rangle - \langle \lambda, \frac{\partial G\left(U_p, p\right)}{\partial p_k} \delta p_k \rangle \ . \tag{3.20}$$

This can be used to express the gradient of the objective function J

$$\frac{\partial J(p)}{\partial p_k} = \frac{\partial L\left(U_p, \lambda, p\right)}{\partial p_k} = \frac{\partial h\left(U_p, p\right)}{\partial p_k} - \langle \lambda, \frac{\partial G\left(U_p, p\right)}{\partial p_k} \rangle \ . \tag{3.21}$$

Improvement over Finite Differences To calculate the gradient using the adjoint method two PDE solutions are necessary, the solution of the forward equation U_p and the adjoint equation λ. Their solution efforts are typically similar. Additionally the scalar product has to be calculated, but its effort can usually be neglected. In comparison to the calculation of the gradient using finite differences, where $\dim(p) + 1$ PDE solutions are required, the effort can be reduced to two solutions. This is particularly advantageous when the parameter dimension is large.

This improvement can be observed most notably when using a gradient-based optimization approach, in which even multiple evaluations of the gradient are necessary.

3.3 Adjoint Equations for the $\mathcal{M}1$-Model

To use the adjoint method for the gradient of the problem specific objective function, the equations (3.17), (3.19) and (3.21) have to be derived specific to our inverse problem, which includes the $\mathcal{M}1$-Model. This is partially very technical, therefore some steps will be denoted in abbreviated form.

3.3.1 Forward Equation

The forward equation (3.17) has to be solved in order to calculate the physical solution U_p to the given set of parameters p. This is done by evaluating the PDE-constraint $G(U_p, p) = 0$, which in the $\mathcal{M}1$-Model is the model equation (2.1) together with the boundary and initial conditions described in section 2.1.3

$$-\partial_\epsilon(S(p)U_p) + \partial_x F_x(U_p) + \partial_y F_y(U_p) = -T(p)U_p \ . \tag{3.22}$$

3.3.2 Adjoint Equation

We have seen, that descriptions of the terms $\frac{\partial G(U_p,p)}{\partial U}\delta U_p$ and $\frac{\partial G(U_p,p)}{\partial p_k}\delta p_k$ are necessary in equations (3.19) and (3.21). For simplicity we neglect the ∂_y terms in the PDE-constraint G in this derivation, but these can be handled analogously to the ∂_x terms. I will also drop the notation $\cdot(\bar{x},\epsilon)$ for functions of $\bar{x}$ and ϵ and introduce $\cdot(p)$ for quantities depending on the parameter p.

Variations of the Constraint To find the variation of the constraint

$$G(U_p,p) = -\partial_\epsilon(S(p)U_p) + \partial_x F_x(U_p) + T(p)U_p \ , \tag{3.23}$$

we insert $U_p + \delta U_p$ and $p + \delta p$

$$\begin{aligned} &G(U_p+\delta U_p, p+\delta p_k) \\ =& -\partial_\epsilon(S(p+\delta p_k)(U_p+\delta U_p)) + \partial_x F_x(U_p+\delta U_p) + T(p+\delta p_k)(U_p+\delta U_p) \ . \end{aligned} \tag{3.24}$$

For the stopping power S and the transport coefficient T analytical expressions are given, so

$$S(p+\delta p_k) = S(p) + \partial_{p_k} S(p)\delta p_k \qquad \text{and} \tag{3.25}$$

$$T(p+\delta p_k) = T(p) + \partial_{p_k} T(p)\delta p_k \ . \tag{3.26}$$

For the flux function F_x we use a linearization and write

$$F_x(U_p+\delta U_p) \approx F_x(U_p) + DF_x(U_p)\delta U_p \ . \tag{3.27}$$

Combining equation 3.24 with equations 3.25, 3.26 and 3.27 yields for the variation

$$G(U_p+\delta U_p, p+\delta p_k) = G(U_p,p) + \frac{\partial G(U_p,p)}{\partial U}\delta U_p + \frac{\partial G(U_p,p)}{\partial p_k}\delta p_k + \mathcal{O}(||\delta U_p \delta p||) \ , \tag{3.28}$$

where

$$\frac{\partial G(U_p,p)}{\partial U}\delta U_p = -\partial_\epsilon(S(p)\delta U_p) + \partial_x(DF_x(U_p)\delta U_p) + T(p)\delta U_p \tag{3.29}$$

$$\frac{\partial G(U_p,p)}{\partial p_k}\delta p_k = [-\partial_\epsilon(\partial_{p_k} S(p)U_p) + \partial_{p_k} T(p)U_p]\delta p_k \ . \tag{3.30}$$

Variations of the Objective Functional Since we need expressions for $\langle \frac{\delta h(U_p,p)}{\delta U}, \delta U_p\rangle$ and $\frac{\partial h(U_p,p)}{\partial p_k}\delta p_k$, variations of the objective functional also are necessary. Therefore the dependency of the k-ratios $k^{i,j}$ from U_p is needed (section 1). For simplification of following equations I will introduce a post-processing operator $R^{i,j}$, that computes the k-ratios for a given U

$$k^{i,j} = R^{i,j}(U) \ . \tag{3.31}$$

The operator R has the form (cf. section 1.5 and 1.6)

$$R^{i,j}(U) = \int_{\epsilon_{cutoff}}^{\epsilon_{initial}} \int_{\Omega} \xi^{i,j}(\bar{x}, \epsilon) u_1(\bar{x}, \epsilon) \, \mathrm{d}x \, \mathrm{d}\, \epsilon \ , \tag{3.32}$$

where $\xi^{i,j}$ is a scalar that accounts for the physical quantities from section 1. Then the objective function can be written as

$$h(U_p, p) = \sum_{i,j} \frac{1}{2} (R^{i,j}(U_p) - \tilde{k}^{i,j})^2 \ . \tag{3.33}$$

Inserting the perturbations δp_k and δU_p into equation (3.33) yields

$$h(U_p + \delta U_p, p + \delta p_k) = \sum_{i,j} \frac{1}{2} (R^{i,j}(U_p + \delta U_p, p + \delta p_k) - \tilde{k}^{i,j})^2 \ . \tag{3.34}$$

Using the linearity of R in U, the bionomial theorem and the similarity of the operator R to the scalar product in $\mathbb{U}$, equation (3.34) can be transformed to

$$h(U_p + \delta U_p, p + \delta p_k) = h(U_p, p) + \langle \frac{\delta h(U_p, p)}{\delta U}, \delta U_p \rangle + \frac{\partial h(U_p, p)}{\partial p_k} \delta p_k + \mathcal{O}(||\delta U_p \delta p||) \ , \tag{3.35}$$

where

$$\langle \frac{\delta h(U_p, p)}{\delta U}, \delta U_p \rangle = \langle \begin{pmatrix} \sum_{i,j} (R^{i,j}(U_p, p) - \tilde{k}^{i,j}) \xi^{i,j}(\bar{x}, \epsilon, p) \\ 0 \\ 0 \end{pmatrix}, \delta U_p \rangle \tag{3.36}$$

$$\frac{\partial h(U_p, p)}{\partial p_k} \delta p_k = \sum_{i,j} [(R^{i,j}(U_p, p) - \tilde{k}^{i,j}) \partial_{p_k} R^{i,j}(U_p, p)] \delta p_k \ . \tag{3.37}$$

The derivative of the post-processing operator $\partial_{p_k} R^{i,j}$ reads

$$\partial_{p_k} R^{i,j}(U_p, p) = \int_{\epsilon_{cutoff}}^{\epsilon_{initial}} \int_{\Omega} \partial_{p_k} \xi^{i,j}(p) u_{1,p} \, \mathrm{d}x \, \mathrm{d}\, \epsilon \ . \tag{3.38}$$

The derivative of the scalar $\xi^{i,j}(p)$ is

$$\partial_{p_k} \xi^{i,j}(p) = \frac{\sigma^{i,j}_{emiss}}{I^{i,j}_{std}} \left(e^{-\int_{d(\bar{x})} \mu(y, E^{i,j}) \, \mathrm{d}y} \partial_{p_k} N^i_V(\bar{x}) + N^i_V(\bar{x}) e^{-\int_{d(\bar{x})} \partial_{p_k} \mu(y, E^{i,j}) \, \mathrm{d}y} \right) \ , \tag{3.39}$$

where the remaining derivatives with respect to p_k are calculated based on case decisions regarding the grid cells and elements.

Adjoint Operator For the calculation of the adjoint state variable λ, the adjoint operator $\frac{\partial G}{\partial U}^*$ has to be derived. With equation (3.29) we can replace $\frac{\partial G(U_p, p)}{\partial U} \delta U_p$ in equation (3.18)

$$\langle \lambda, \frac{\partial G(U_p, p)}{\partial U} \delta U_p \rangle = \langle \lambda, -\partial_\epsilon (S(p) \delta U_p) + \partial_x (DF_x(U_p) \delta U_p) + T(p) \delta U_p \rangle \ . \tag{3.40}$$

To find the adjoint operator, δU_p must be isolated so that all operators act on λ. I will treat each linearization independently and use partial integration to relocate the partial derivatives. For the

first summand

$$\begin{aligned}\langle\lambda, -\partial_\epsilon\left(S\left(p\right)\delta U_p\right)\rangle &= -\int_{\epsilon_{cutoff}}^{\epsilon_{initial}}\int_\Omega \lambda^T\partial_\epsilon\left(S\left(p\right)\delta U_p\right)\mathrm{d}x\,\mathrm{d}\epsilon \\ = -\left[\int_\Omega \lambda^T S\left(p\right)\delta U_p\,\mathrm{d}x\right]_{\epsilon_{cutoff}}^{\epsilon_{initial}} &+ \int_{\epsilon_{cutoff}}^{\epsilon_{initial}}\int_\Omega \partial_\epsilon\left(\lambda^T\right)S\left(p\right)\delta U_p\,\mathrm{d}x\,\mathrm{d}\epsilon \\ = -\left[\int_\Omega \lambda^T S\left(p\right)\delta U_p\,\mathrm{d}x\right]_{\epsilon_{cutoff}}^{\epsilon_{initial}} &+ \langle S\left(p\right)\partial_\epsilon\lambda, \delta U_p\rangle\ .\end{aligned} \tag{3.41}$$

For the second summand

$$\begin{aligned}\langle\lambda, \partial_x\left(DF_x\left(U_p\right)\delta U_p\right)\rangle &= \int_{\epsilon_{cutoff}}^{\epsilon_{initial}}\int_\Omega \lambda^T\partial_x\left(DF_x\left(U_p\right)\delta U_p\right)\mathrm{d}x\,\mathrm{d}\epsilon \\ = \int_{\epsilon_{cutoff}}^{\epsilon_{initial}}\left[\int_{y_0}^{y_1}\lambda^T DF_x\left(U_p\right)\delta U_p\,\mathrm{d}x\right]_{x_0}^{x_1} &- \int_\Omega \partial_x\lambda^T DF_x\left(U_p\right)\delta U_p\,\mathrm{d}x\,\mathrm{d}\epsilon \\ = \int_{\epsilon_{cutoff}}^{\epsilon_{initial}}\left[\int_{y_0}^{y_1}\lambda^T DF_x\left(U_p\right)\delta U_p\,\mathrm{d}x\right]_{x_0}^{x_1}\mathrm{d}\epsilon &- \langle DF_x\left(U_p\right)^T\partial_x\lambda, \delta U_p\rangle\ .\end{aligned} \tag{3.42}$$

And for the third summand, with $T\left(p\right)^T = T\left(p\right)$

$$\begin{aligned}\langle\lambda, T\left(p\right)\delta U_p\rangle &= \int_{\epsilon_{cutoff}}^{\epsilon_{initial}}\int_\Omega \lambda^T T\left(p\right)\delta U_p\,\mathrm{d}x\,\mathrm{d}\epsilon \\ &= \int_{\epsilon_{cutoff}}^{\epsilon_{initial}}\int_\Omega \left(T\left(c\right)\lambda\right)^T\delta U_p\,\mathrm{d}x\,\mathrm{d}\epsilon \\ &= \langle T\left(c\right)\lambda, \delta U_p\rangle\ .\end{aligned} \tag{3.43}$$

Requiring the boundary integrals arising from partial integration to be zero, after summation the adjoint operator $\frac{\partial G(U_p,p)}{\partial U}^*$ is obtained

$$\begin{aligned}&\langle\lambda, \frac{\partial G\left(U_p,p\right)}{\partial U}\delta U_p\rangle \\ =&\langle S\left(p\right)\partial_\epsilon\lambda - DF_x\left(U_p\right)^T\partial_x\lambda + T\left(p\right)\lambda, \delta U_p\rangle = \langle\frac{\partial G\left(U_p,p\right)}{\partial U}^*\lambda, \delta U_p\rangle\ .\end{aligned} \tag{3.44}$$

The requirenment to set the boundary integrals to zero will be discussed later.

Adjoint Equation From equations (3.36) and (3.44) we identify all parts of the adjoint equation, we have to solve for λ

$$\frac{\delta h\left(U_p,p\right)}{\delta U} - \frac{\partial G\left(U_p,p\right)}{\partial U}^*\lambda = 0\ , \tag{3.45}$$

$$S\left(p\right)\partial_\epsilon\lambda - DF_x\left(U_p\right)^T\partial_x\lambda + T\left(p\right)\lambda = \begin{pmatrix}\sum_{i,j}(R^{i,j}(U_p,p) - \tilde{k}^{i,j})\xi^{i,j}(\bar{x},\epsilon,p) \\ 0 \\ 0\end{pmatrix}\ . \tag{3.46}$$

Like the $\mathcal{M}1$-Model, the adjoint equation is also a hyperbolic partial differential equation, therefore we can use the theory developed in section 2.2 to solve for the adjoint state variable λ.

Adjoint Initial and Boundary Conditions In the derivation of the adjoint equation, the boundary integrals were demanded to be zero. To meet the first requirement

$$-\left[\int_\Omega \lambda^T S\left(p\right)\delta U_p \,\mathrm{d}x\right]_{\epsilon_{cutoff}}^{\epsilon_{initial}} = 0 \tag{3.47}$$

the integral over the domain Ω has to be zero at energies ϵ_{cutoff} and $\epsilon_{initial}$. At initial energy $\epsilon_{initial}$ the solution $U(\bar{x}, \epsilon_{initial})$ is defined by its initial condition. Therefore also a perturbation $U(\bar{x}, \epsilon_{initial}) + \delta U(\bar{x}, \epsilon_{initial})$ equals the same initial condition. We can conclude

$$\delta U(\bar{x}, \epsilon_{initial}) = 0 \quad \forall \bar{x} \in \Omega \ . \tag{3.48}$$

At cutoff energy ϵ_{cutoff} no statement about δU is possible and we have to demand for the adjoint state variable

$$\lambda(\bar{x}, \epsilon_{cutoff}) = 0 \quad \forall \bar{x} \in \Omega \ . \tag{3.49}$$

This yields an initial condition for the adjoint state variable. Its definition is at the opposite site of the energy interval $[\epsilon_{cutoff}, \epsilon_{initial}]$, therefore we have to calculate the adjoint state variable backwards.

The second requirement

$$\int_{\epsilon_{cutoff}}^{\epsilon_{initial}} \left[\int_{y_0}^{y_1} \lambda^T DF_x\left(U_p\right)\delta U_p \,\mathrm{d}x\right]_{x_0}^{x_1} \mathrm{d}\epsilon \tag{3.50}$$

yields boundary conditions for λ. In section 2.1.3 two different boundary conditions for the $\mathcal{M}1$-Model were introduced. None of them was congruous to the model equations, thus we were not able to construct correct boundary conditions for the adjoint state variable. Similar to the initial condition it can be reasoned, that if U_p is fixed at the boundary, $\delta U_p = 0$ and the bounary integral vanishes, but then no statement would be possible for λ. As a workaround we suggest to extrapolate λ at the boundary. These conditions still produce acceptable results if none of the electrons travel close to the boundary (cf. section 3.4).

3.3.3 Scalar Product

To calculate the gradient of the objective function, we have to combine the adjoint variable with the solution as derived in equation (3.21)

$$\frac{\partial J(p)}{\partial p_k} = \frac{\partial h\left(U_p, p\right)}{\partial p_k} - \langle \lambda, \frac{\partial G\left(U_p, p\right)}{\partial p_k} \rangle \ . \tag{3.51}$$

With the $\mathcal{M}1$-Model specific terms derived in equation (3.29) and (3.36) the scalar product reads

$$\frac{\partial J(p)}{\partial p_k} = \sum_{i,j} (R^{i,j}(U_p, p) - \tilde{k}^{i,j}) \partial_{p_k} R^{i,j}(U_p, p) - \langle \lambda, (-\partial_\epsilon(\partial_{p_k} S(p) U_p) + \partial_{p_k} T(p) U_p) \rangle \ . \tag{3.52}$$

Knowing U_p and λ, this expression can be directly calculated yielding the derivative for each parameter p_k, which can then be combined to the gradient of the objective function $\nabla_p J(p)$.

3.4 Optimization using the Adjoint Method

Notes on the Implementation The implementation of the FV-Method to solve the $\mathcal{M}1$-Model is mostly based on the Python library CLAWPACK [5], which uses FORTRAN procedures as its base. The Riemann solver (section 2.2.3) is provided as FORTRAN Code, while the solver initialization and call is implemented in Python. The methods to solve the adjoint model follow the same path. All other calculations are written in Python employing the library NumPy. The methods available in SciPy were used for the optimization.

While mathematical methods tend to be implemented in a procedural way, we implemented the physical routines object-oriented, such that they can be extended or replaced by other implementations.

Plot of the Gradient As a test case the example of a homogeneous material from section 3.1 is considered. As the objective function for this problem only depends on the mass concentration of the material, the gradient reduces to the derivative with respect to the only parameter. In figure 18 the objective function is shown together with the gradient calculated with the finite difference approach and the adjoint method.

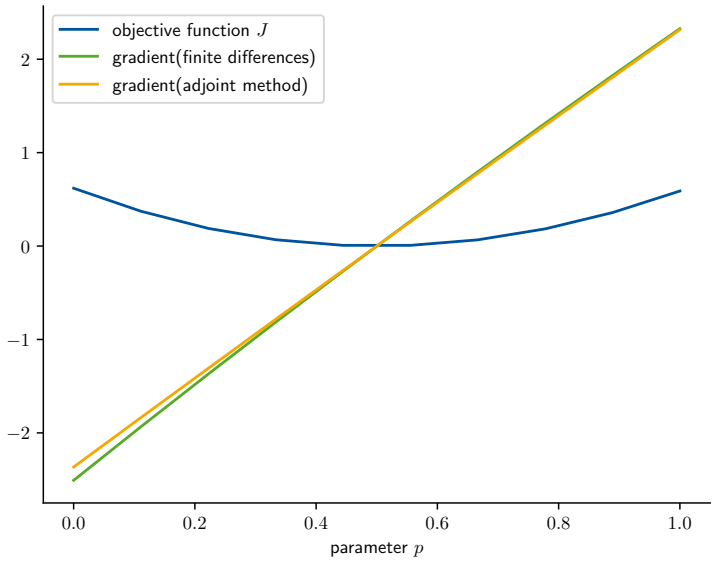

Figure 18: Gradient of the objective function of a homogeneous material

In this plot both methods provide similar values for the derivative. For $p \to 0$ the values for the gradient differ more strongly, due to improper use of boundary values. $p \to 0$ means the material contains more chromium, which has a lower stopping power, therefore electrons travel closer to or beyond the boundary.

Optimization Example To construct an optimization example, we use the setting with multiple concentrations on a 4×4 grid inside the domain from section 3.1. In this example the detector is moved to the top left corner of the sample $[-300\text{nm}, 0\text{nm}]$. Together with the optimization algo-

rithms from SciPy[13], the reference parameters $p^{ref} = (0.4, 0.6, 0.7, 0.2)^T$ could be reconstructed from initial values $p = 0.5$. The error $||p^k - p^{ref}||$ of the parameters to the reference parameters is shown over the iteration step in figure 19. In different color the error in each of the four parameters is shown. The errors of parameter p_1 and p_3 decrease faster because their grid cells are closer to the materials surface and the impact point of the electron beam.

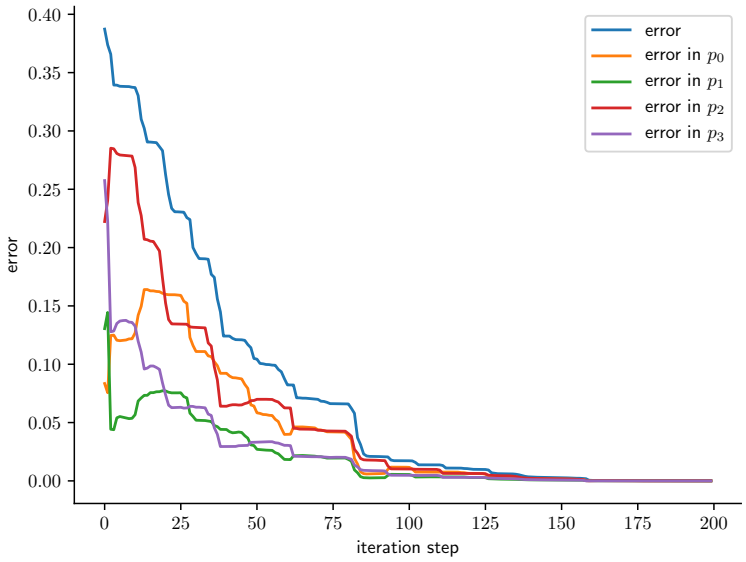

Figure 19: Plot of the errors for each iteration step of the optimization

In figure 20 the path of the optimization is plotted on top of the objective function for parameters p_0, p_1 and p_0, p_2.

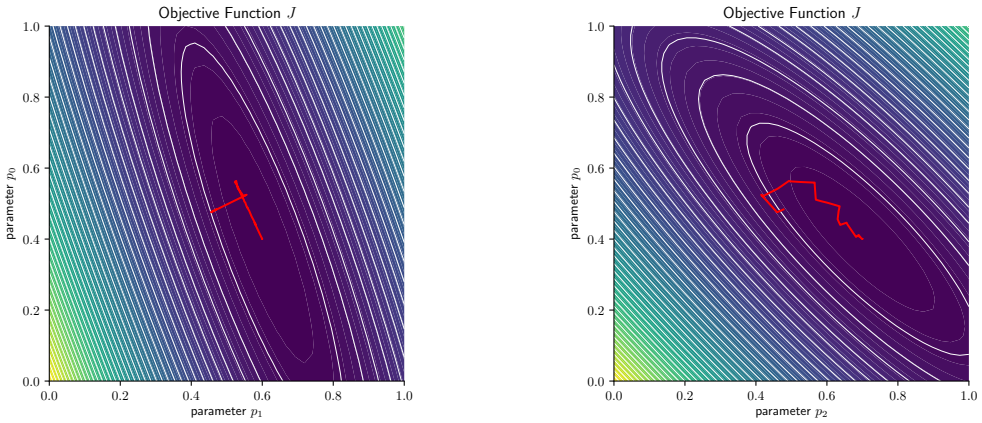

Figure 20: The iteration steps of the optimization

Occasionally the parameters move away from the minimum, but the objective function plots were created with the other parameters (p_2/p_3 or p_1/p_3) fixed to its reference values, while in the optimization all four parameters were variable. In the end the minimum is found exactly.

Conclusion and Outlook

Conclusion With the aim to improve the spatial resolution in electron probe microanalysis the inverse problem of reconstruction using a k-ratio model based on the $\mathcal{M}1$-Model has been investigated. In this work, a solver for the $\mathcal{M}1$-Model and the modelling of k-ratios are presented, an objective function based on this k-ratio model is analyzed and the chemical composition of a sample is reconstructed. Under suitable conditions (electron beam positions/energies) the objective function reveals a unique minimum. The volumes in which the mass concentrations vary can be smaller than the interaction volume of the beam electrons. Mass concentrations in a small area of the sample were reconstructed using gradient based optimization methods. To calculate the gradient of the objective function, the adjoint state method offers a fast alternative to finite differences. It allowed us to run the optimization on a conventional notebook in acceptable time, despite the fact, that computational performance was not the primary goal during the implementation of this method.

To accomplish a physical solution, our choice of boundary conditions should be reconsidered. At the moment they are physically unfounded, but suitable to model the electron beam because the error introduced by the boundary conditions is sufficiently small. Even though alternative boundary and initial conditions to describe the electron beam should be derived which are congruous to the equations of the $\mathcal{M}1$-Model.

Outlook The objective function used in this work was based on artificial measurements, calculated by the same model as used in the reconstruction. This allowed us to reconstruct perfectly. Real measurements from experiments include noise and models have a certain error. As a result, the objective function could have a more inaccurate, misleading minimum or several local minima. The effects of noisy measurements and model errors on the objective function should be investigated.

Nevertheless, the presented method allowes studies on the shape and minima of the objective function and the reconstructability of finely dissolved chemical compositions. Furthermore, the application of the developed reconstruction algorithm should also be considered in a real experiment.

I would like to thank my supervisor Jonas Bünger for introducing me to this topic, for the many discussions during my time as a research assistant on his project and my bachelor thesis. Many thanks to my professor Manuel Torillhon, who taught my mathematics lecture almost every semester during my studies and accepted me into his research group.

References

[1] E. Anderson, Z. Bai, C. Bischof, S. Blackford, J. Demmel, J. Dongarra, J. Du Croz, A. Greenbaum, S. Hammarling, A. McKenney, and D. Sorensen. *LAPACK Users' Guide*. Society for Industrial and Applied Mathematics, Philadelphia, PA, third edition, 1999. ISBN 0-89871-447-8 (paperback).

[2] Derek S. Bale, Randall J. LeVeque, Sorin Mitran, and James A. Rossmanith. A wave propagation method for conservation laws and balance laws with spatially varying flux functions. *SIAM Journal on Scientific Computing*, 24(3):955–978, 2003. doi: 10.1137/S106482750139738X. URL `https://doi.org/10.1137/S106482750139738X`.

[3] Christophe Berthon, Pierre Charrier, and Bruno Dubroca. An hllc scheme to solve the m 1 model of radiative transfer in two space dimensions. *Journal of Scientific Computing*, 31 (3):347–389, Jun 2007. ISSN 1573-7691. doi: 10.1007/s10915-006-9108-6. URL `https://doi.org/10.1007/s10915-006-9108-6`.

[4] Jonas Buenger, Silvia Richter, and Manuel Torrilhon. A deterministic model of electron transport for electron probe microanalysis. *IOP Conference Series: Materials Science and Engineering*, 304:012004, 01 2018. doi: 10.1088/1757-899X/304/1/012004.

[5] Clawpack Development Team. Clawpack software, 2017. URL `http://www.clawpack.org`. Version 5.4.0.

[6] R Duclous, B Dubroca, and M Frank. A deterministic partial differential equation model for dose calculation in electron radiotherapy. *Physics in Medicine & Biology*, 55(13):3843, 2010. URL `http://stacks.iop.org/0031-9155/55/i=13/a=018`.

[7] Nicolas Ralph Gauger. *Das Adjungiertenverfahren in der aerodynamischen Formoptimierung*. PhD thesis, Nov 2003. URL `https://publikationsserver.tu-braunschweig.de/receive/dbbs_mods_00001550`.

[8] Jonathan B. Goodman and Randall J. LeVeque. A geometric approach to high resolution tvd schemes. *SIAM Journal on Numerical Analysis*, 25(2):268–284, 1988. doi: 10.1137/0725019. URL `https://doi.org/10.1137/0725019`.

[9] Amr G. Guaily and Marcelo Epstein. Boundary conditions for hyperbolic systems of partial differentials equations. *Journal of Advanced Research*, 4(4):321 – 329, 2013. ISSN 2090-1232. doi: https://doi.org/10.1016/j.jare.2012.05.006. URL `http://www.sciencedirect.com/science/article/pii/S2090123212000355`.

[10] J. H. Hubbell, P. N. Trehan, Nirmal Singh, B. Chand, D. Mehta, M. L. Garg, R. R. Garg, Surinder Singh, and S. Puri. A review, bibliography, and tabulation of k, l, and higher atomic shell x-ray fluorescence yields. *Journal of Physical and Chemical Reference Data*, 23(2):339–364, 1994. doi: 10.1063/1.555955. URL `https://doi.org/10.1063/1.555955`.

[11] J. H. Hubbell, P. N. Trehan, Nirmal Singh, B. Chand, D. Mehta, M. L. Garg, R. R. Garg, Surinder Singh, and S. Puri. Erratum: "a review, bibliography, and tabulation of k, l, and higher atomic shell x-ray fluorescence yields" [j. phys. chem. ref. data 23, 339 (1994)]. *Journal of Physical and Chemical Reference Data*, 33(2):621–621, 2004. doi: 10.1063/1.1756152. URL `https://doi.org/10.1063/1.1756152`.

[12] J.H. Hubbell and S.M. Seltzer. Tables of x-ray mass attenuation coefficients and mass energy-absorption coefficients (version 1.4). National Institute of Standards and Technology, Gaithersburg, MD, 2004. [Online] Available: http://physics.nist.gov/xaamdi.

[13] Eric Jones, Travis Oliphant, Pearu Peterson, et al. SciPy: Open source scientific tools for Python, 2001. URL http://www.scipy.org/.

[14] Randall J. LeVeque. Balancing source terms and flux gradients in high-resolution godunov methods: The quasi-steady wave-propagation algorithm. *Journal of Computational Physics*, 146(1):346 – 365, 1998. ISSN 0021-9991. doi: https://doi.org/10.1006/jcph.1998.6058. URL http://www.sciencedirect.com/science/article/pii/S0021999198960582.

[15] R.J. LeVeque. *Finite Volume Methods for Hyperbolic Problems*. Cambridge Texts in Applied Mathematics. Cambridge University Press, 2002. ISBN 9780521009249. URL https://books.google.de/books?id=QazcnD7GUoUC.

[16] R.J. LeVeque. *Numerical Methods for Conservation Laws*. Lectures in Mathematics. ETH Zürich. Birkhäuser Basel, 2012. ISBN 9783034886291. URL https://books.google.de/books?id=2ZAkBAAAQBAJ.

[17] Kyle T Mandli, Aron J Ahmadia, Marsha Berger, Donna Calhoun, David L George, Yiannis Hadjimichael, David I Ketcheson, Grady I Lemoine, and Randall J LeVeque. Clawpack: building an open source ecosystem for solving hyperbolic pdes. *PeerJ Computer Science*, 2: e68, 2016. doi: 10.7717/peerj-cs.68.

[18] Niklas Mevenkamp. Inverse modeling in electron probe microanalysis based on deterministic transport equations. Master's thesis, RWTH Aachen University, 09 2013. URL http://www.mathcces.rwth-aachen.de/_media/3teaching/00projects/2013_masterthesis_niklasmevenkamp.pdf.

[19] P. Monreal and M. Frank. Higher order minimum entropy approximations in radiative transfer. *ArXiv e-prints*, December 2008.

[20] Ludovic Métivier and the SEISCOPE group. Numerical optimization and adjoint state methods for large-scale nonlinear least-squares problems. Joint Inversion Summer School Barcelonnette, France, 2015.

[21] Nhan T Nguyen. Continuous adjoint-based optimization of hyperbolic equations with nonlinear differential equation constraints on periodic boundary conditions. *Preprint*.

[22] R.-E. Plessix. A review of the adjoint-state method for computing the gradient of a functional with geophysical applications. *Geophysical Journal International*, 167(2):495–503, 2006. doi: 10.1111/j.1365-246X.2006.02978.x. URL http://dx.doi.org/10.1111/j.1365-246X.2006.02978.x.

[23] G.C. Pomraning. The fokker-planck operator as an asymptotic limit. *Mathematical Models and Methods in Applied Sciences*, 02(01):21–36, 1992. doi: 10.1142/S021820259200003X. URL https://www.worldscientific.com/doi/abs/10.1142/S021820259200003X.

[24] C.J. Powell. Cross sections for inelastic electron scattering in solids. *Ultramicroscopy*, 28(1): 24 – 31, 1989. ISSN 0304-3991. doi: https://doi.org/10.1016/0304-3991(89)90264-7. URL http://www.sciencedirect.com/science/article/pii/0304399189902647.

[25] L. Reimer. *Scanning Electron Microscopy: Physics of Image Formation and Microanalysis*. Springer Series in Optical Sciences. Springer, 1998. ISBN 9783540639763. URL https://books.google.de/books?id=0Fm3T6F6_LEC.

[26] B. Schmidtmann and M. Torrilhon. A Hybrid Riemann Solver for Large Hyperbolic Systems of Conservation Laws. *ArXiv e-prints*, July 2016.

[27] E.F. Toro. *Riemann Solvers and Numerical Methods for Fluid Dynamics: A Practical Introduction*. Springer Berlin Heidelberg, 2009. ISBN 9783540498346. URL https://books.google.de/books?id=SqEjX0um8o0C.

[28] D. Werner. *Funktionalanalysis*. Springer-Lehrbuch. Springer Berlin Heidelberg, 2011. ISBN 9783642210174. URL https://books.google.de/books?id=jCAkBAAAQBAJ.

[29] L. C. Wilcox, G. Stadler, T. Bui-Thanh, and O. Ghattas. Discretely exact derivatives for hyperbolic PDE-constrained optimization problems discretized by the discontinuous Galerkin method. *ArXiv e-prints*, November 2013.

[30] James H. Wittke. Electron Microanalysis Core Facility Class Notes Signals. https://nau.edu/CEFNS/Labs/Electron-Microprobe/GLG-510-Class-Notes/Signals. Accessed: 2018-08-06.